Green synthesized Cu-doped CeO_2 nanoparticles for Congo red dye adsorption and antibacterial action

Aleena Norbert[1], Surya Mary A[1], Sareen Sarah John[2], Sadasivan Shaji[3], Mohan Jacob[4], Rachel Reena Philip*[,1]

[1] Thin Film Research Lab, Department of Physics, Union Christian College, Aluva, Kerala, India

[2] Department of Biosciences, Union Christian College, Aluva, Kerala, India

[3] Facultad de Ingenieria Mecanica Y Electrica, Universidad Autonoma de Nuevo Leon, Av. Universidad s/n, Cd. Universitaria, San Nicolas de los Garza, Nuevo Leon, 66455, Mexico.

[4] College of Science & Engineering, James Cook University, Australia.

*Corresponding author email id : reenatara@gmail.com orcid id : 0000-0001-8210-0045

Abstract

The removal of pollutants from water bodies is crucial for the well-being of humanity and is a topic of global research. Researchers have turned their attention to green synthesized nanoparticles for wastewater treatment due to their eco-friendly nature, biocompatibility, and cost-effectiveness. This work demonstrates the efficient removal of organic dye and both gram-positive and gram-negative bacteria from water bodies using copper-doped cerium oxide nanoparticles synthesized with *Murraya Koenigii* extract. Characterized via various methods, the 15% copper doped cerium oxide nanoparticles (Cu 15% NPs) exhibited maximum Congo red dye adsorption (98% degradation in 35 minutes). Kinetic analysis favoured a pseudo-second-order model, indicating the chemical nature of adsorption. Equilibrium adsorption isotherms aligned with the Langmuir model, indicating homogenous monolayer dye adsorption on the doped adsorbent. The maximum uptake of adsorbate, Q_m obtained from Langmuir model for Cu 15% NPs was 193 mg/g. The study also showed enhanced antibacterial activity against *Bacillus subtilis, Staphylococcus aureus, Escherichia coli and Pseudomonas aeruginosa* for Cu-doped ceria, attributed to generation of reactive oxygen species (ROS) induced by the redox cycling between Ce^{3+} and Ce^{4+}. This substantiated that the green synthesized copper doped cerium oxide nanoparticles are potential candidates for adsorptive removal of Congo red dye and as antibacterial agents.

Keywords

Green synthesis, Congo red, Cu doped CeO_2, *Murraya Koenigii* , adsorption, antibacterial activity

1. Introduction

The protection of water resources is a global pressing concern as a consequence of population growth and current economic development. About 2 million tons of toxic waste pollutants consisting of organic materials, soluble inorganic compounds, dyes, heavy metals and microorganisms are released into our water resources every day [1,2]. The release of unused dyes from the textile, printing and dyeing industries is the primary cause of water contamination. The majority of the dyes are not biodegradable and potentially dangerous due to the presence of stable aromatic rings. Congo red is such a popular and typical azo dye based on benzidine that is widely used in textile and printing industries. The highly soluble nature of Congo red in water makes it readily dispersed in aquatic resources depending upon the pH value [3]. Due to its toxicity, this widely used pollutant from water bodies must be removed or minimized to permissible levels. Biological pollutants are also dominant in contaminated water along with the physical and chemical pollutants. The biological pollutants consist of pathogenic microorganisms like viruses, bacteria and protozoa which cause chronic and intense health issues [4]. Hence, the treatment of water to remove it to reduce its harmful impact on human beings, animals and agriculture is a hot subject of research in material science and environmental science.

Various physical, chemical and biological techniques have been developed to manage the dye emissions and to remove dyes from water. Some conventional techniques include membrane filtration, ion exchange, precipitation, biological treatment, electrochemical treatment and adsorption [5,6]. Among these techniques, adsorption is a promising method because of its high removal capability, ease of handling and economic feasibility [7]. The selectivity and adsorption capacity of an adsorbent mainly depends on its porosity, increased surface area, pH, number of active sites on the surface, and electrostatic and weak interactions between the adsorbent and dye molecules [8]. Multifarious adsorbents with large surface areas like silica, activated carbon, palygorskite, kaolinite, magnetic nanocomposites and carbon nanotubes are used to remove dyes from water [9]. However, not all of these adsorbents are widely used due to their high cost and difficulty for disposal and regeneration.

CeO_2 nanoparticles (NPs) have gained significant attention as a potential solution for environmental remediation and catalysis due to (i) their low price and superabundance, (ii) high stability, wide bandgap and non-toxicity (iii) outstanding storage and release of oxygen with the reversible redox transition between Ce^{3+} and Ce^{4+} (iv) the possibility to form solid solutions with other oxides and (v) high adsorption efficiency [10,11]. However, research is ongoing to improve the adsorption efficiency of CeO_2 by tuning its surface features with the help of dopants like metal ions that can enhance its interfacial redox activity and create oxygen vacancies. Joshy *et al* [12] synthesized pure CeO_2 and Er^{3+} doped CeO_2 NPs using sol-gel and sol-hydrothermal methods and investigated their adsorption capacity using Congo red, methylene blue and methyl orange. They found that the Er^{3+} doped CeO_2 NPs synthesized by the sol-gel method were very efficient (99.75% removal in 15 minutes) and highly selective towards Congo red. Mousavi-Kamazani *et al* [13] introduced Cu-doped CeO_2 nanostructures as a dual-functional photocatalytic adsorbent. Their 5 wt% Cu-doped CeO_2 flower-like nanostructures were found to adsorb more than 99% of methyl orange in 45 minutes.

Nanoparticles can be prepared using chemical, physical and biological techniques [14,15]. However, the physicochemical methods widely used for making nanoparticles, such as hydrothermal synthesis, sol-gel, homogeneous precipitation and thermal decomposition, have some disadvantages. They often involve toxic chemicals and solvents that are nondegradable. For this reason, green synthesis techniques that involve plants, microbes and other biological products have become popular among researchers. These methods are environment-friendly, biocompatible and cost-effective [16,17]. Among those bio-entities, plants are mostly used for the large-scale synthesis of stable metal and metal oxide-based nanomaterials due to their abundance, non-toxicity and presence of metabolites which act as the reducing and stabilizing agents [18]. Green chemistry synthesis using plant extracts has been a subject of intense research in recent years. It presents an opportunity to design and develop innovative techniques to produce novel nanomaterials or nanohybrid composites with unique properties for energy, environmental and biomedical applications [19–22]. For instance, Kaur *et al* [23] reported the synthesis of silver nanoparticle – tin zirconium (IV) molybdophosphate (AgNP-SnZrMoP) nanocomposite using mulberry leaf extract for the disinfection and detoxification of water. This nanocomposite effectively removed Ba^{2+} ions from wastewater and had a higher antimicrobial efficacy on both gram negative (*E.coli*) and gram positive (*Bacillius*) bacterial strains. Various plant species such as *Gloriosa superba, Moringa oleifera, Aloe barbadensis miller, Jatropha curcus* and

Azadirachta indica have been found to be useful in the synthesis of CeO_2 NPs [24–28]. Although considerable research has been done on green-synthesized metal oxide-based nanomaterials, there are only very few reports on the adsorption studies of green-synthesized CeO_2-based nanomaterials. Curry leaf, the leaves of the curry tree (*Murraya koenigii*), is a native to India with well-known medicinal and culinary applications. Known for its highly aromatic and unique flavor, it is rich in alkaloids, flavonoids, phenolic compounds, acridinecarbazole and carotenoids, which are responsible for its antimicrobial, antifungal, anti-oxidative, antiulcer, anti-inflammatory, cytotoxic and anti-cholesterolemic properties [29]. These properties of curry leaves can enhance the potential of ceria in their antibacterial and medical applications if used for the green synthesis of ceria nanoparticles.

The aim of this study is to investigate the impact of Cu-doping and reduction using curry leaves on modifying the properties of ceria nanoparticles, to enhance their effectiveness in waste water treatment and antibacterial applications. This innovative method of preparation has been successful in tuning the surface properties of CeO_2, leading to a significant improvement in its adsorption efficacy compared to previous synthesis techniques. The research data has been analyzed using adsorption isotherms and kinetic models to gain a better understanding of the process. A comprehensive structural, morphological and compositional analysis, together with theoretical evaluation, has been conducted to assess the following: (i) the enhancement in adsorption with Cu-doping and the type of sorption, (ii) the effect of doping on surface characteristics such as surface area and porosity, (iii) the active role of Ce^{3+}, Ce^{4+}, Cu^{2+}, Cu^{1+} redox reactions in antibacterial activity, and (iv) the effect on adsorption and antibacterial activity due to the induction of more oxygen vacancies on doping.

2. Experimental Section

2.1. Preparation of curry leaf extract

Curry leaves, also known as *Murraya Koenigii* leaves, are collected from various locations in Ernakulam district, South India. The leaves are washed thoroughly with distilled water, and 30gm of the leaves is boiled in 100 mL of distilled water at 80^0C for 10 minutes. The extract is then strained using Whatman grade No.1 filter paper and refrigerated for further studies.

2.2. Synthesis of CeO_2 NPs

To synthesize CeO_2 NPs, a simple green method is used and it is illustrated in figure 1. First, 0.1 M of cerium nitrate hexahydrate (($Ce_2(NO_3)_3.6H_2O$), Himedia) is dissolved in 40 mL of distilled water with constant stirring. Next, 10 mL of curry leaf extract is added to the solution and stirred continuously for 30 minutes. The resulting solution is heated at 80^0 C on a hot plate until the supernatant has vaporized. The derived powder is then pounded into fine particles and calcinated at 600^0 C for 2 hours.

2.3. Synthesis of Cu-doped CeO_2 NPs

To synthesize Cu-doped CeO_2 NPs, copper doped CeO_2 NPs entitled Cu 5%, Cu 10% and Cu 15% are prepared by adding 5, 10 and 15wt% of copper (II) sulfate pentahydrate (($CuSO_4.5H_2O$), Merck) to the 0.1 M of $Ce_2(NO_3)_3.6H_2O$ solution and following the aforementioned growth route.

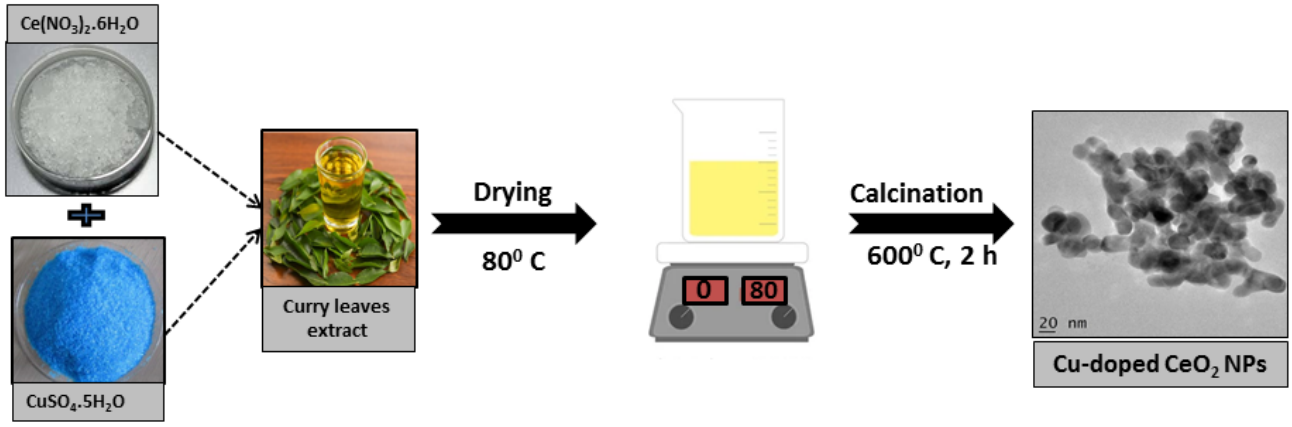

Figure 1. Schematic illustration of the synthesis procedure of Cu-doped CeO_2 NPs

2.4. Preparation of dye solution

The dye solution for adsorption studies is prepared by dissolving 1mg of Congo red (Sigma-Aldrich) in 100mL distilled water. In a similar way, concentrations between 1 to 5mg are prepared.

2.5. Characterizations

The size and crystal structure of the nanoparticles are studied from X-ray diffractograms (XRD) taken using Bruker D8 Advance X-ray diffractometer with CuKα radiation (λ = 1.5406 Å). The Raman spectroscopic study is carried out utilizing a Thermo Scientific DXR Raman microscope having a 532 nm excitation laser wavelength. The functional groups are analyzed using Fourier-transform infrared (FTIR) Thermo Nicolet iS50 spectrometer in the range 400-4000 cm^{-1}. The elemental compositions in the samples are estimated by energy dispersive analysis of X-rays (EDAX) utilizing JEOL JED 2300 unit. X-ray photoelectron spectroscopy (XPS) measurements are accomplished with Thermo scientific XPS equipment having an Al anode X-ray source (AlKα) and the peak locations are fitted using XPSPEAK 4.1 software. The morphological studies are done by Carl Zeiss Sigma field emission scanning electron microscope (FESEM) and Jeol/JEM 2100 high-resolution transmission electron microscope (HRTEM). The specific surface area and the pore size distribution of the samples are calculated from the Brunauer-Emmett-Teller (BET) and Barrett-Joyner-Halenda (BJH) method using a Belsorp high precision gas/vapor adsorption apparatus by N_2 adsorption. The optical studies are performed with diffuse reflectance Perkin Elmer Lambda 365 UV Vis NIR Spectrophotometer in the range 200-1000nm.

2.6. Adsorption studies

For adsorption studies, 1mg of the ceria sample is introduced into 5mL of Congo red dye solution (1mg per 100mL, pH ~6.5) and kept in an ultrasonicator in dark condition. At intervals of 5 minutes, the sample is separated from the solution using centrifugation and the supernatant is analyzed by UV-Vis spectrophotometer. The percentage of removal efficiency is calculated using equation (1) as:

$$\text{Percentage of removal efficiency} = \frac{C_o - C_t}{C_o} \times 100 \qquad (1)$$

where C_0 is the initial concentration of the dye solution and C_t is the concentration after a time interval.

To explore the adsorption kinetic studies, Pseudo-first and second order models are used. Langmuir

and Freundlich adsorption isotherms are utilized to analyze the adsorption equilibrium by varying the initial concentration of dye as 1, 2, 3 and 5mg per 100mL. The adsorbed amount of dye on the samples at time t is calculated from equation (2):

$$Q_t = \frac{(C_o - C_t)V}{m} \quad (2)$$

where C_o is the initial concentration (mgL^{-1}), C_t is the concentration of Congo red dye solution at time t (mgL^{-1}), V is the volume of the Congo red solution (L) and m is the mass of the adsorbent (g). The adsorption isotherm experiments are performed by varying the initial dye concentrations (1, 2, 3 and 5 mg per 100mL) keeping the mass of the adsorbent constant (1mg in 5ml dye solution) [30]. When the equilibrium is reached, the remaining liquid phase concentration of Congo red is assessed by its maximum absorption value.

Besides adsorption studies, the photocatalytic efficiency of the prepared ceria in pure and doped forms have been tested (Supplementary information). The absorbance measurements (figure S1 and S2) are done on the dye solution for checking the photocatalytic degradation efficiency in addition to adsorptive efficiency for dye removal.

2.7. Antibacterial studies

The antibacterial activity of the synthesized nanoparticles is examined on four pathogenic bacteria like the gram-positive *Staphylococcus aureus* (MTCC.740) and *Bacillus subtilis* (MTCC.736) and the gram-negative *Pseudomonas aeruginosa* (MTCC.5210) and *Escherichia coli* (MTCC.443) using agar well diffusion method as explained in our previous work [22]. The clear areas around the wells are measured to evaluate the diameter of the inhibition zones and to compare the activity of the samples on different bacteria.

3. Results and discussions

3.1. Structural analysis

The X-ray diffraction (XRD) patterns of CeO_2 and Cu-doped CeO_2 nanoparticles are presented in figure 2. The diffraction peaks located at angles (2θ) of 28.54^0, 33.08^0, 47.50^0, 56.38^0, 59.12^0, 69.46^0, 76.76^0 and 79.13^0 corresponding to the (111), (200), (220), (311), (222), (400), (331) and (420) planes, respectively. These peaks indicate the formation of cubic fluorite type CeO_2 nanoparticles as per the JCPDS card no. 034-0394. The pure CeO_2 nanoparticles have a high crystalline character, with intense and sharper diffraction peaks. They show a highly preferential orientation of the grains along the (111) plane when compared to the Cu-doped CeO_2 nanoparticles. There is no formation of any secondary phase in the XRD patterns of the pure CeO_2 and Cu 5% doped sample. Peaks associated with hexagonal Ce_2O_3 or $Ce(OH)_3$ are not present here, which indicates the complete transformation of the sample into cubic fluorite ceria [31].

The presence of additional minor diffraction peaks in Cu 10% and Cu 15% samples at 2θ of 35.84^0 and 38.99^0 indicates the presence of a monoclinic CuO along with ceria when the dopant percentage is increased. The peaks correspond to (111) and (002) planes of monoclinic CuO (JCPDS card no. 045-0937). The Cu-related peaks are not detected in the Cu 5% sample. This along with other characterizations proposes that a secondary phase of CuO is developed with increased dopant addition; while Cu is successfully incorporated into the CeO_2 lattice without any other phase formation for smaller dopant concentrations.

The peak positions, crystallite sizes (D=14.7±0.6), lattice constant (a=5.41±0.02Å) and unit cell volume (V=158.3±0.3) of the doped and undoped samples do not show any appreciable changes. This can be attributed to the antagonistic effect of the lowering of lattice constant due to Cu incorporation to the counter effect of lattice expansion due to the formation of greater ionic radii Ce^{3+} by Ce^{4+} reduction [22]. The replacement of larger Ce ions with Cu having a lower valence state and smaller ionic radius decreases the number of Ce^{4+} ions significantly and increases Ce^{3+} ions progressively along with oxygen vacancy formation [32,33]. The strain developed in the CeO_2 lattice, determined from the Williamson-Hall (W-H) plot as shown in figure 3, is found to be increasing from $4.3*10^{-4}$ to

$9.9*10^{-4}$ with increasing Cu dopant concentration. This is expected since lattice modifications will occur with the accommodation of dopant atoms in the cation site which also aids in the formation of oxygen vacancies.

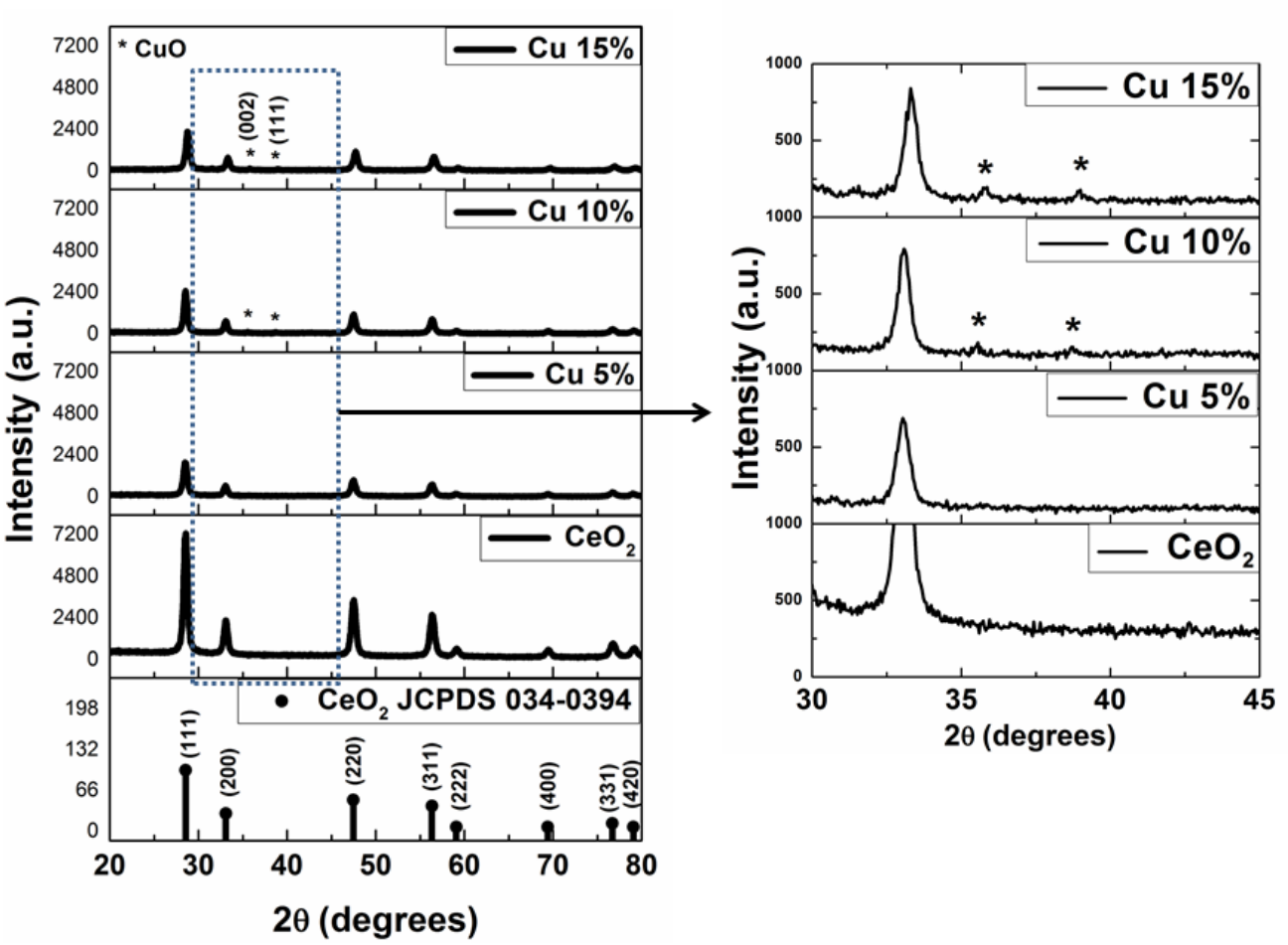

Figure 2. X-ray diffraction (XRD) patterns of CeO_2 NPs and Cu-doped CeO_2 NPs

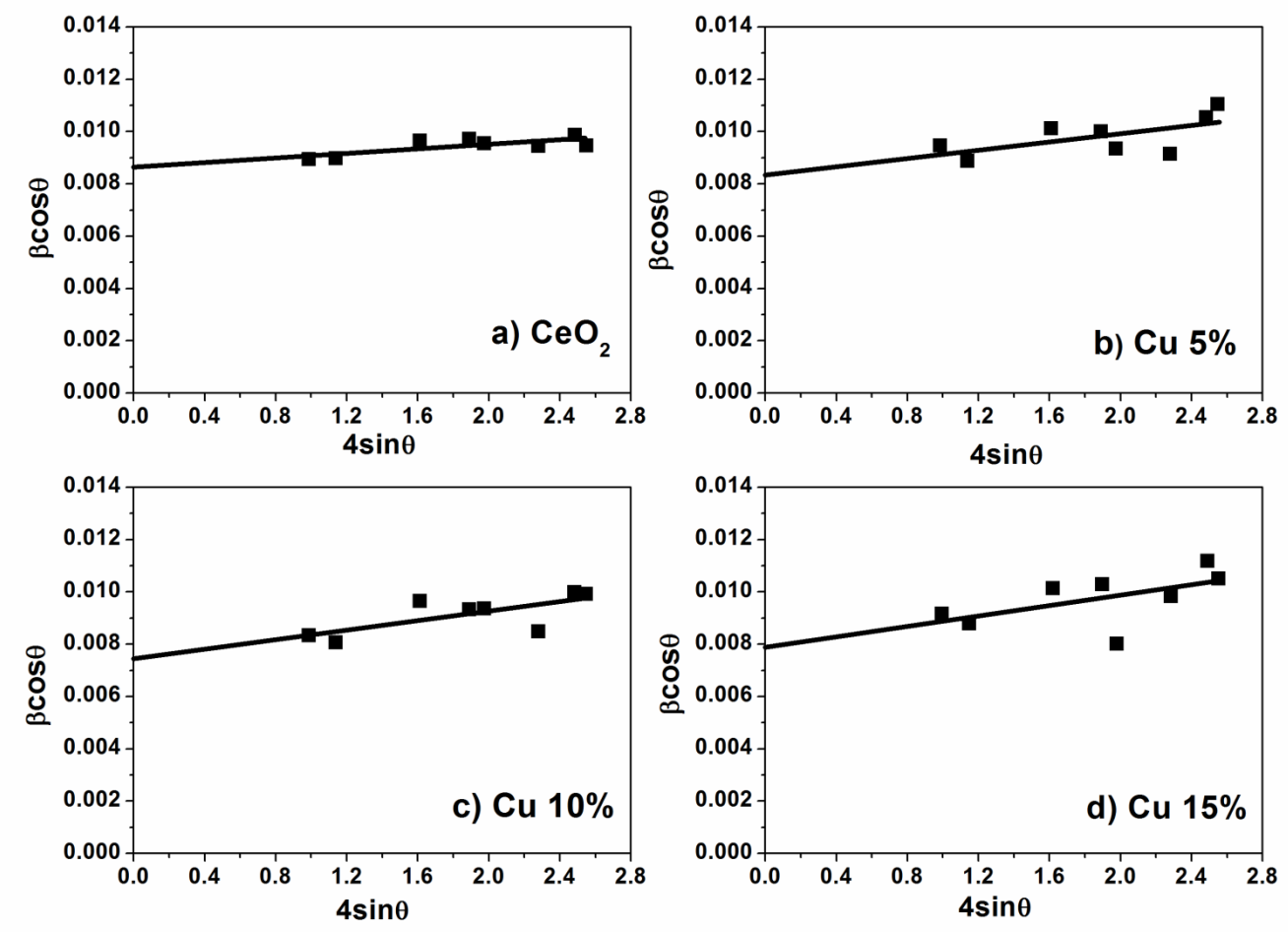

Figure 3. Williamson-Hall plot of CeO_2 NPs and Cu-doped CeO_2 NPs

Raman spectroscopy is utilized to gain information on the different types of defects that are created or induced in the CeO_2 lattice by Cu-ion doping. Figure 4 presents the typical and normalized Raman spectrum of pure and Cu-doped CeO_2 NPs. The most intense peak at 460 cm^{-1} is attributed to the symmetrical stretching mode (F_{2g}) of Ce-O lattice vibrations, which is the characteristic Raman frequency of cubic fluorite CeO_2 structures. It is susceptible to non-stochiometry induced in the oxygen sub-lattice as a result of any molecular disorder in the local environment around Ce. Compared to the Raman spectrum of pure CeO_2, this mode is slightly shifted to lower wavenumbers (447, 443 and 437 cm^{-1} for Cu 5, 10 and 15%) and becomes wider with increasing Cu-doping concentration. Moreover, the F_{2g} peak of CeO_2 is perfectly symmetric with respect to Cu-doped samples. An asymmetry in peak profile, along with a decrease in intensity, is observable in the doped. This red shift and broadening are due to slight lattice distortions on doping and the creation of framework defects particularly the oxygen vacancies (O_v) [33]. The small peaks at ~ 250, 600 and 1100 cm^{-1} represent the

second order defect-induced (D) transverse acoustic modes of CeO_2. The peak at ~600 cm^{-1}, which is evident in the doped samples, signifies the defect related to oxygen vacancies in the CeO_2 lattice because of the presence of Ce^{3+} ions [34,35]. The concentration of oxygen vacancies appears to increase with the increase in dopant concentration.

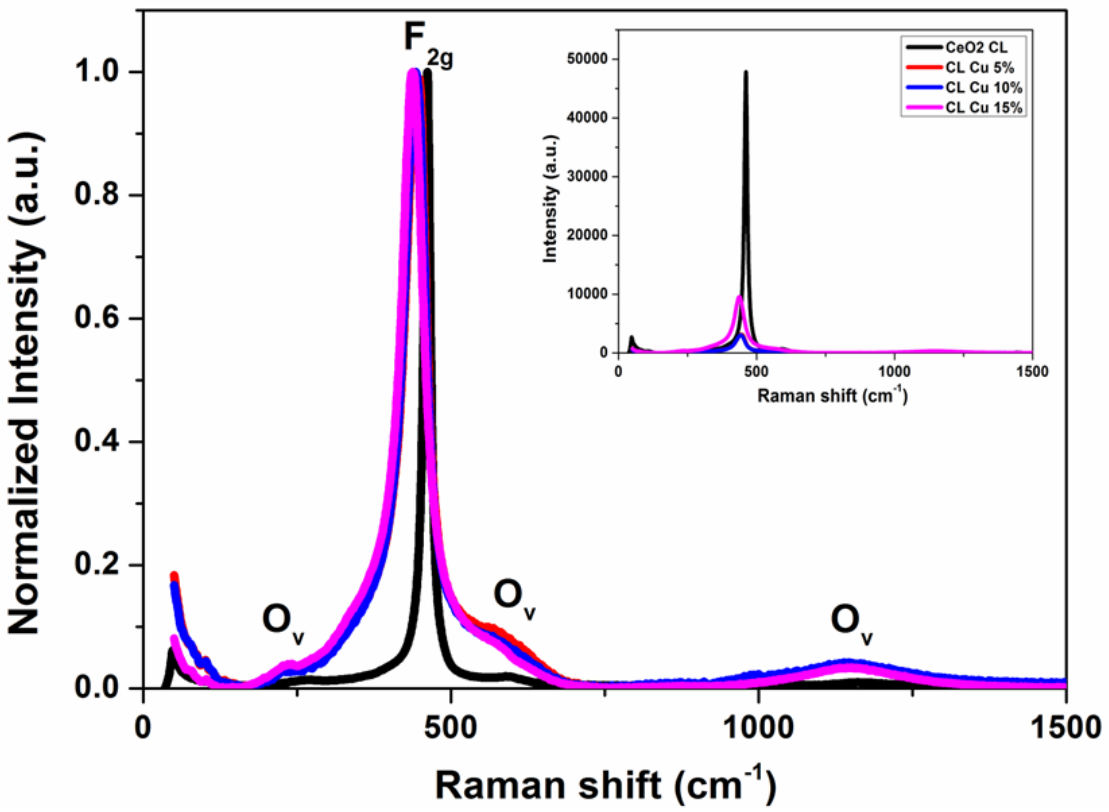

Figure 4. Typical and normalized Raman spectrum of pure CeO_2 and Cu-doped CeO_2 NPs

The Fourier-transform infrared (FTIR) spectra of curry leaves extract, pure and Cu-doped CeO_2 NPs are depicted in figure 5. The FTIR helps to identify the various characteristic functional groups present in each sample, as well as the proteins and phenolic compounds in the curry leaves extract. The peaks in the low wavenumber region of 700-750 cm^{-1} correspond to the lattice stretching vibration modes of Ce-O [36]. This band is present in pure and doped ceria, although slight shifts due to the effect of strain and vacancy formations on doping are found in their peak positions. The weak peak at 601 cm^{-1} in the Cu-doped samples corresponds to Cu-O stretching along the [101] direction, while the peak at 650 cm^{-1} corresponds to O-Cu-O vibrations of Cu substituted at the Ce site in ceria lattice (see the expanded region of the spectra) [37,38]. No peaks are observable in this region in the spectrum of pure

ceria. This specifies the incorporation of Cu into the lattice forming O-Cu-O bonds and the formation of the CuO secondary phase. The observation is consistent with XRD, EDAX, XPS and TEM analysis.

The bands around 3400 cm^{-1} found in all the samples and curry leaves extract are due to O-H stretching, which is caused by residual alcohols, water, phenolic compounds and proteins present in the curry leaves extract. Similarly, the peaks at 2850 and 2925 cm^{-1} are due to asymmetric and symmetric stretching of C-H bonds. The peak around 1600 cm^{-1} corresponds to the H-O-H bending vibration mode that overlay with the band in compliance with the O-C-O stretching. This peak also indicates the presence of the N-H primary amines or Amide II band [29]. The band in the region around 1400 cm^{-1} can be attributed to the carbonate-type species that interact with the cerium cations on the surface [39]. The bands in the region 1100-1300 cm^{-1} correlate with the CH_3 mode of organic moieties. The band around 1050 cm^{-1} is associated with the C-OH stretching and OH bending vibrations [29].

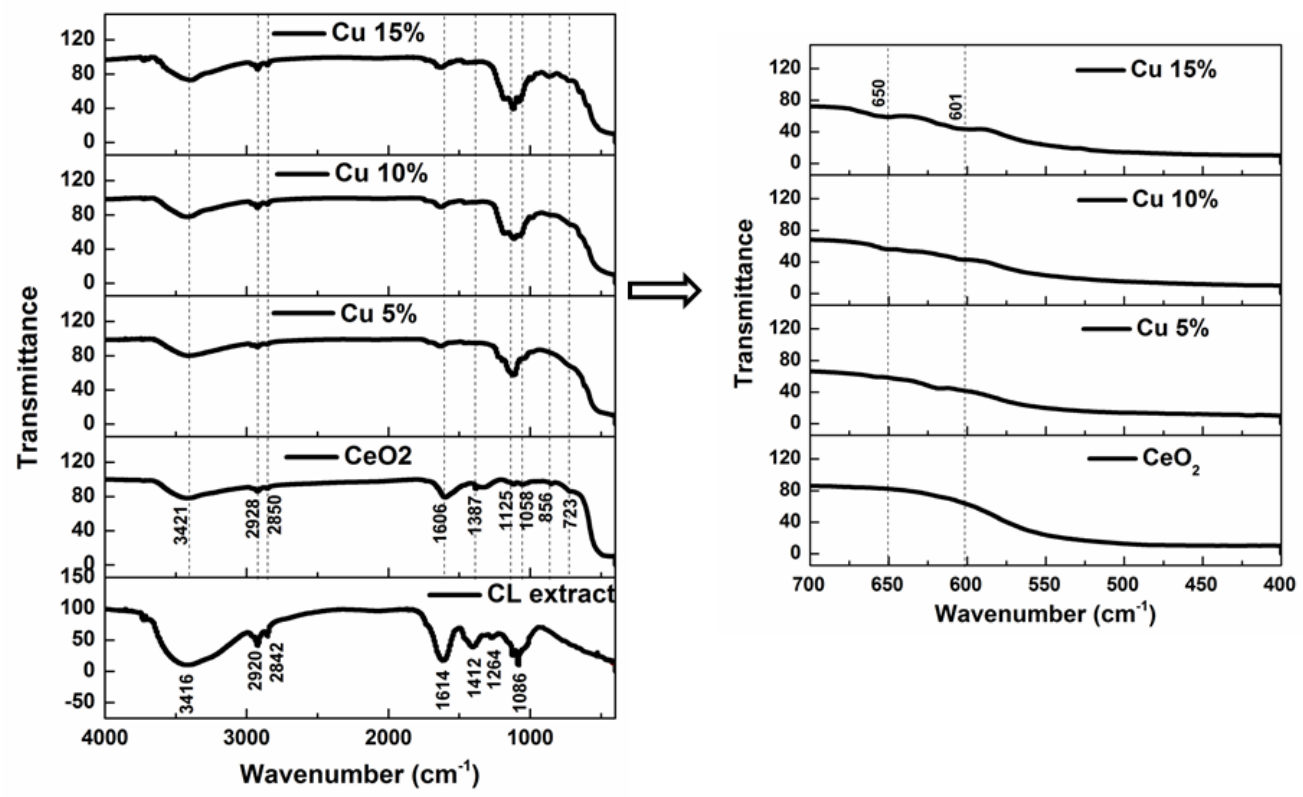

Figure 5. FTIR spectra of CeO_2 NPs and Cu-doped CeO_2 NPs

3.2. Morphological and microstructure analysis

Figure 6 presents the field emission scanning electron microscopy (FESEM) micrographs of CeO_2 and Cu 15% doped CeO_2 NPs. These images provide information on surface morphology and the extent of agglomeration. The FESEM images of both pure and doped CeO_2 NPs display agglomerations of various sizes with mesoporous structures. The Cu 15% doped sample exhibit a highly porous structure with more dispersed agglomerated structures compared to pure CeO_2 NPs. The highly porous structure of Cu 15% doped CeO_2 NPs can be the reason for its high adsorptive behaviour.

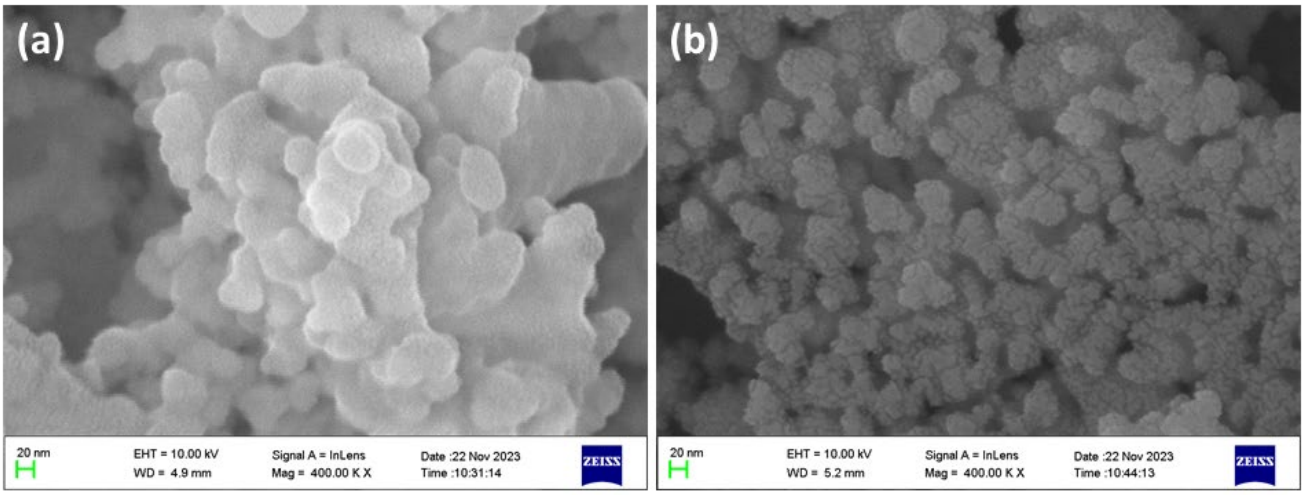

Figure 6. FESEM images of (a) CeO_2 NPs and (b) Cu 15% doped CeO_2 NPs

The transmission electron microscope (TEM) images and selected area electron diffraction (SAED) patterns of CeO_2 and Cu 15% doped CeO_2 nanoparticles are shown in figure 7. Both pure and Cu 15% doped samples show tetra-sided grains with smooth edges, and some grains have sharp edges. The average size of the pure CeO_2 and Cu 15% doped CeO_2 nanoparticles are ~20 nm, according to the TEM analysis. The high-resolution transmission electron microscope (HRTEM) images show well-resolved lattice fringes of (111) planes with d-spacing values of 3.0 Å and 3.1 Å for cerium oxide in pure CeO_2 and Cu 15% doped CeO_2 nanoparticles, respectively. The SAED pattern of the pure CeO_2 sample in figure 7(c) shows several Debye-Scherrer diffraction rings attributed to the (111), (200), (220) and (311) crystal planes of cubic fluorite CeO_2. The SAED pattern of Cu 15% doped CeO_2 sample in figure 7(f) demonstrates the (111), (200), (222), (331), (311) and (220) crystal planes of cubic fluorite CeO_2 and the (002) plane of monoclinic CuO. These observations support the structural

and compositional characterizations.

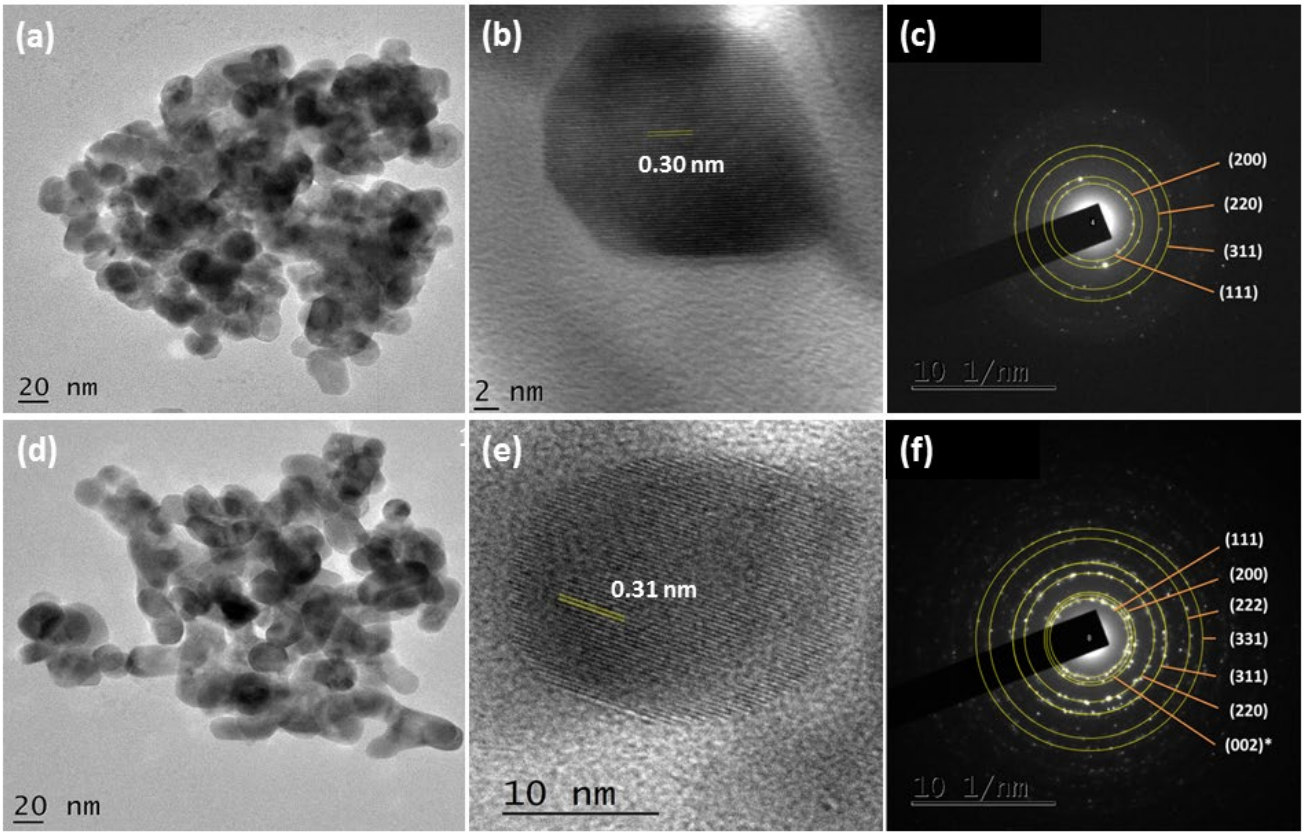

Figure 7. TEM, HRTEM and SAED images of (a-c) CeO_2 NPs and (d-f) Cu 15% doped CeO_2 NPs

3.3. Specific surface area analysis

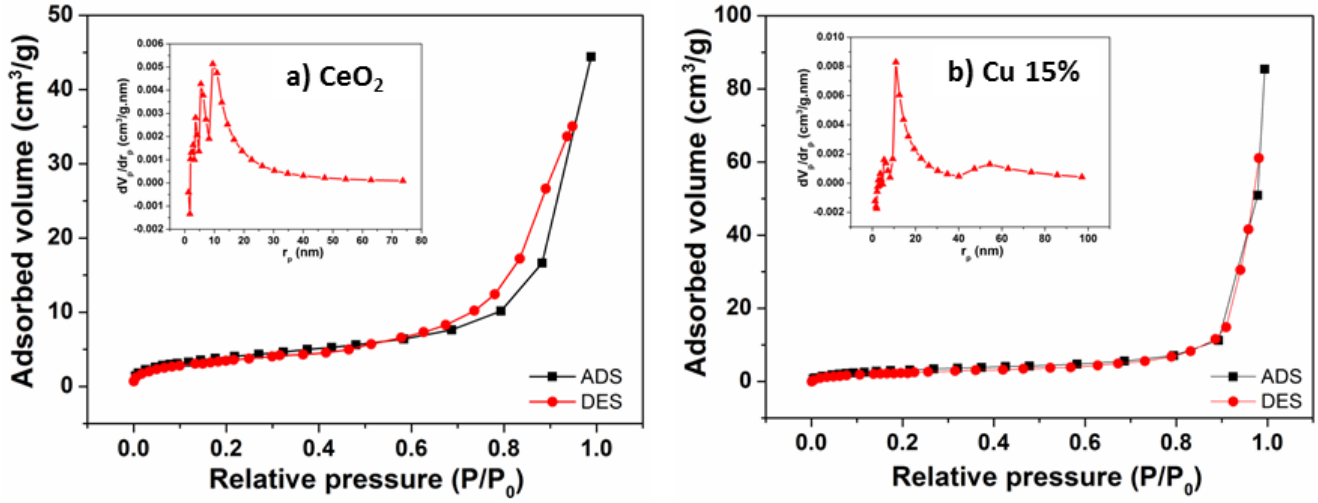

Figure 8. N_2 adsorption-desorption isotherms and Pore size distributions (inset) of (a) CeO_2 NPs and (b) Cu 15% doped CeO_2 NPs

Table 1. Results of BET analysis for CeO_2 and Cu-doped CeO_2 NPs

Sample	**BET surface area (m^2g^{-1})**	**Pore volume (cm^3g^{-1})**	**Pore diameter (nm)**
CeO_2	14.62	0.0687	18.80
Cu 15%	11.21	0.1184	42.27

The N_2 adsorption-desorption isotherms of pure CeO_2 and Cu 15% nanoparticles are shown in figure 8 and the obtained specific surface area, pore volume and pore diameter are given in Table 1. The average values of the pore diameters between 2nm and 50nm suggest that the samples are mesoporous in nature. The high value of mean pore diameter in the doped, when compared to the pure, must be due to the presence of pores with large as well as small diameters, an observation which aligns with the dv_p/dr_p versus r_p diagram in the inset of figure 8(b). The pores are of different sizes in the doped due to the presence of a secondary phase CuO along with the dominant phase of ceria as mentioned in XRD, XPS and TEM analysis of the doped samples. Moreover, the samples exhibit type IV adsorption with a loop in the vertical region that is typical for a mesoporous adsorbent. However, the adsorption-desorption loop is very narrow in the Cu-doped indicating reduced capillary condensation in these [40]. Since the pore volume bears a direct proportionality to pore diameter and the surface area is an inverse proportionality, the surface area in Cu-doped is slightly lesser than in the pure. The enhanced adsorption capacity of Cu-doped observed may be related to the availability of greater pore volume of the adsorbent.

3.4. Compositional analysis

The chemical composition estimated from energy-dispersive X–ray spectroscopy (EDS) confirms the sample purity and the existence of Ce, Cu and O elements (Supplementary information figure S3). Also, there is a slight increase in the percentage of copper from 3.7→4.4→4.8 at.% with the increase in added Cu concentration respectively from Cu5%→Cu10%→Cu15% which validates the successful doping of Cu. The oxygen content in the Cu-doped samples seems to be decreasing from that of pure CeO_2 NPs to the Cu 15% doped from ~71.4 to 64.7 at.% indicating the existence of a large number of oxygen vacancies in the Cu doped. This is in agreement with the suggestion given in XRD studies, as

well as Raman and XPS studies explained in the latter sections.

Figure 9 represents the X-ray photoelectron spectroscopy (XPS) survey spectrum of CeO_2 NPs and Cu-doped CeO_2 NPs. The peaks in the XPS survey spectrum of CeO_2 are associated with C 1s, O 1s, O 2s, Ce 4s, Ce 5s, Ce 3p, Ce 4p, Ce 3d, Ce 4d and Auger lines. In addition to these peaks, Cu 3s, Cu 2s, Cu $2p_{3/2}$ and Cu $2p_{1/2}$ peaks are detected in Cu-doped CeO_2 NPs.

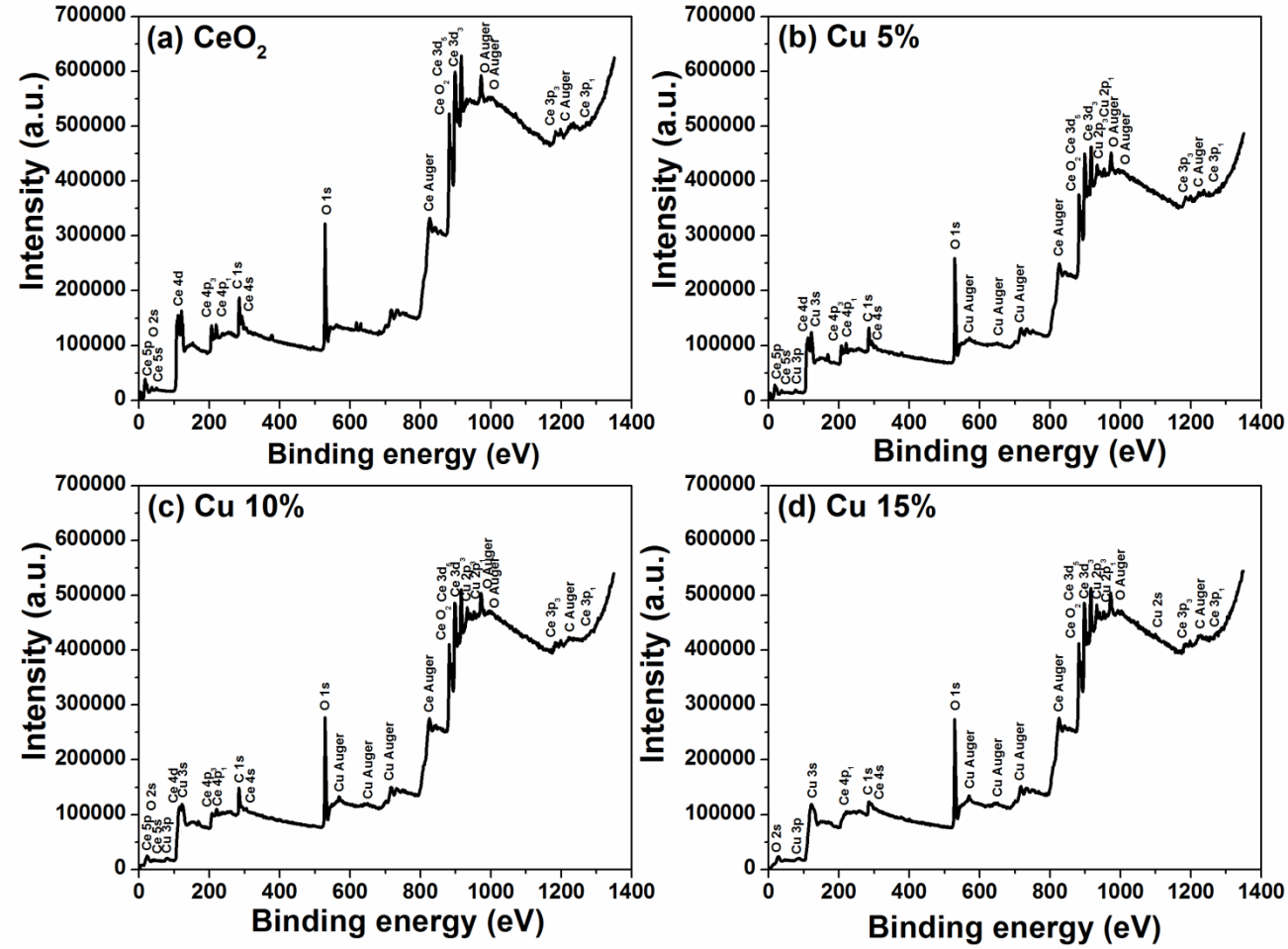

Figure 9. XPS survey spectrum of CeO_2 NPs and Cu-doped CeO_2 NPs

The Ce 3d spectra of CeO_2 NPs and Cu-doped CeO_2 NPs are shown in figure 10. The spectra consist of multiple doublets analogous to the spin-orbit split of $3d_{5/2}$ and $3d_{3/2}$. By using Gaussian fitting, the

Ce 3d spectra are deconvoluted into 10 peaks as given in figure 10. The peaks corresponding to $3d_{3/2}$ and $3d_{5/2}$ are branded as 'u' and 'v' respectively. The peaks designated at u^{III} and v^{III} are the primary lines for $3d_{3/2}$ and $3d_{5/2}$ states, which correspond to the final state of the $3d^{10}4f^0$ configuration of Ce^{4+} ions. The u^{III} and v^{III} lines have two satellites each at u^{II}, u and v^{II}, v which are located close to the lower binding energy region because of the bonding and antibonding states that arise from the electron transfer between the filled O 2p orbital and an empty Ce 4f orbital. The peaks at u_0, u^I,v_0 and v^I represent the $3d^{10}4f^1$ electronic state of Ce^{3+} ions. The presence of these peaks confirms the coexistence of Ce^{4+} and Ce^{3+} ions in the samples [22].

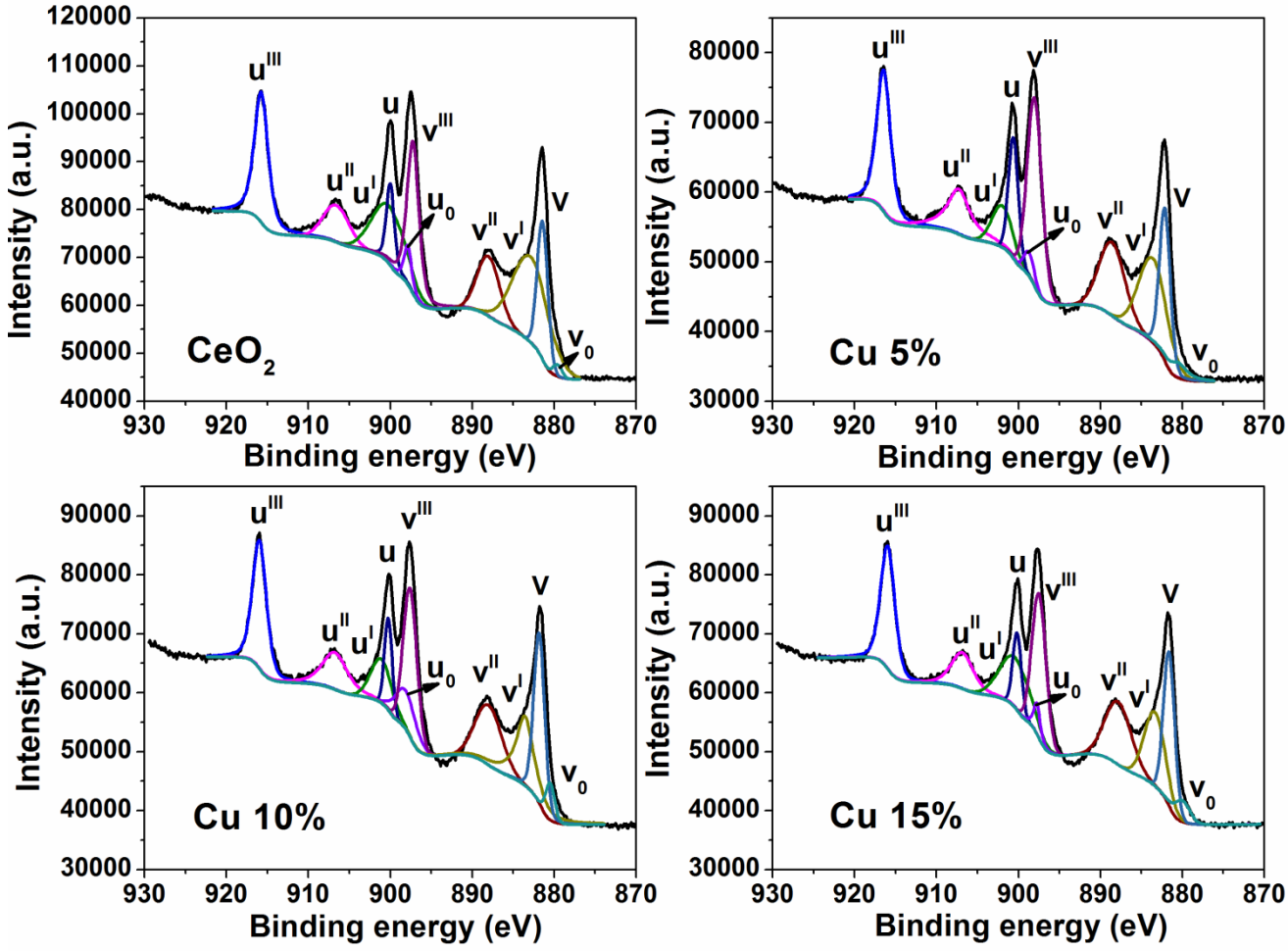

Figure 10. Ce 3d spectra of CeO_2 NPs and Cu-doped CeO_2 NPs

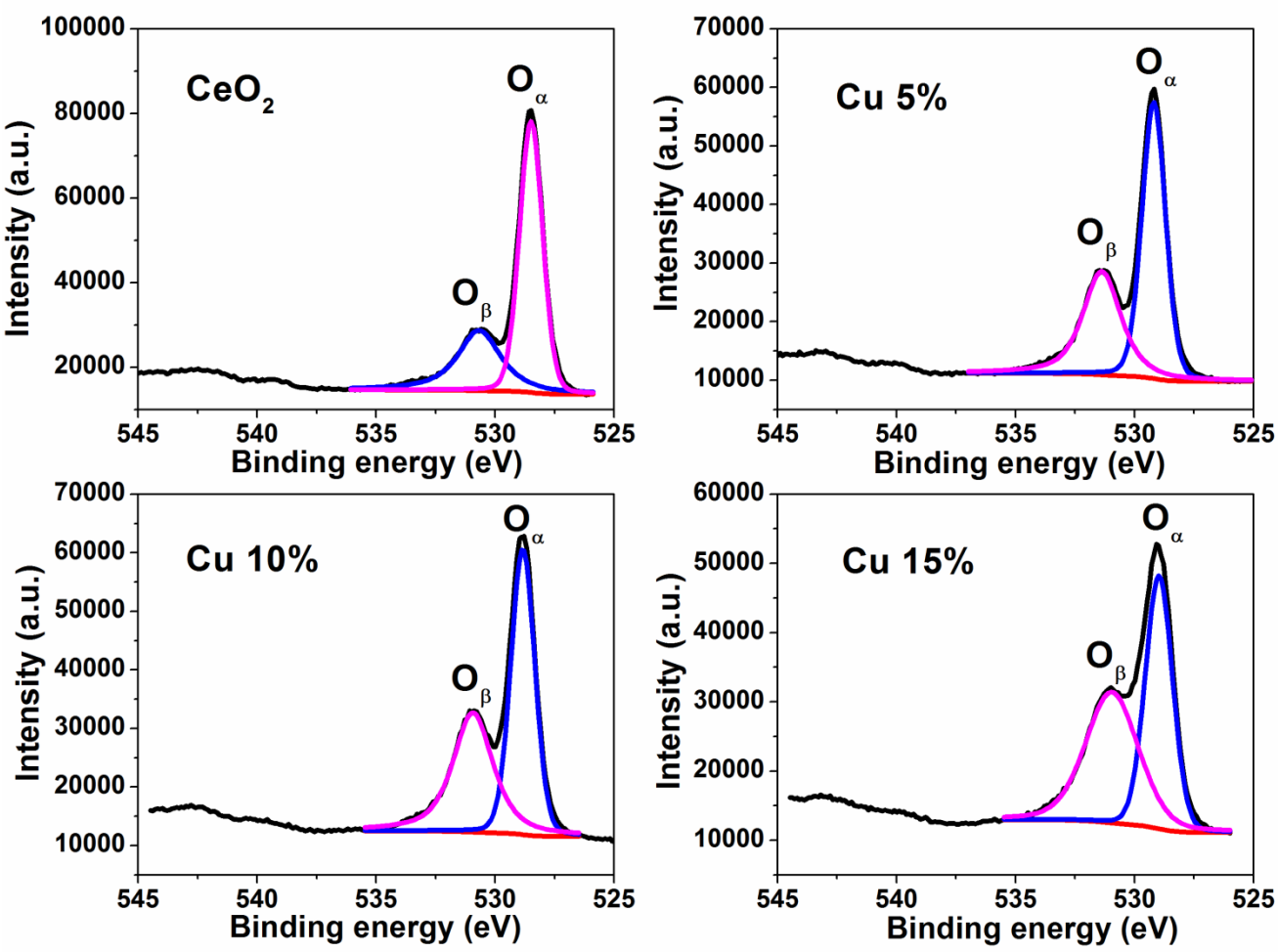

Figure 11. O 1s spectra of CeO_2 NPs and Cu-doped CeO_2 NPs

The O 1s spectra of pure and Cu-doped CeO_2 NPs are shown in figure 11. The peak at 528 eV (O_α) relates to the lattice oxygen and the peak at 530 eV (O_β) relates to the oxygen adsorbed on the nanoparticle surface. With the increase in Cu-dopant concentration, the area of the O_β peak increases suggesting the formation of more oxygen vacancies.

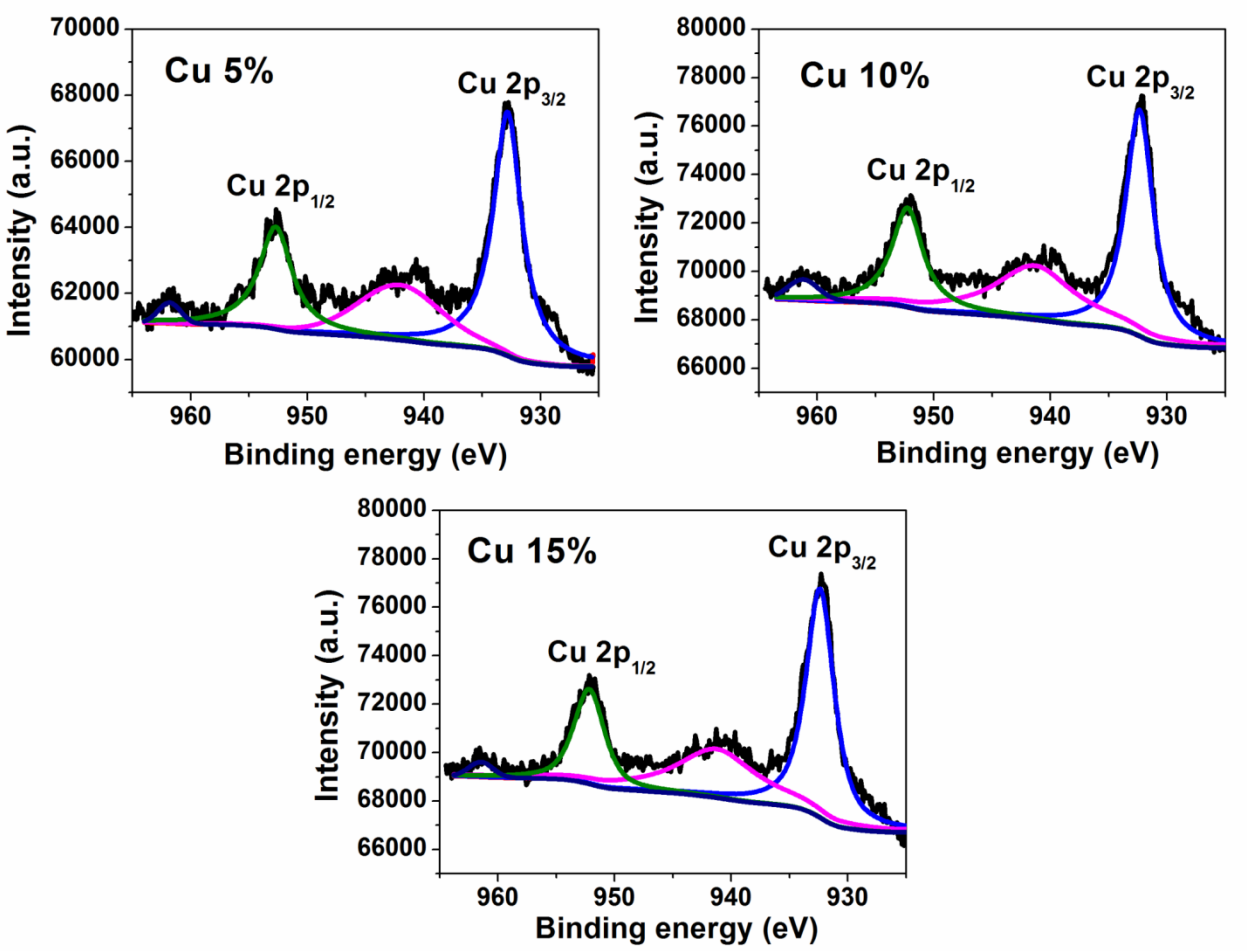

Figure 12. Cu 2p detailed spectra of Cu- doped CeO_2 NPs

The Cu 2p detailed spectra of the Cu-doped samples are given in figure 12. The two Cu 2p peaks found at 932 and 952 eV corresponds to Cu $2p_{3/2}$ and Cu $2p_{1/2}$, respectively. The satellite peak observed at 940 eV is associated with Cu^{2+}, indicating the formation of CuO. The less intense peak detected around 960 eV is due to Cu^{1+}, which might be due to the Cu ions present inside the lattice. The binding energy locations, area and percentage compositions in CeO_2 NPs and Cu-doped CeO_2 NPs estimated from XPS results are given in Table 2.

Table 2. Binding energy locations, area and percentage compositions in CeO_2 NPs and Cu-doped CeO_2 NPs estimated from XPS result.

Sample			CeO_2		Cu 5%		Cu 10%		Cu 15%	
Peaks	Oxidation state		B.E. [eV]	Area	B.E. [eV]	Area	B.E. [eV]	Area	B.E. [eV]	Area
Ce $3d_{3/2}$	4+	u^{III}	915.75	71837	916.45	52579	915.97	54327	915.95	51183
	4+	u^{II}	906.60	30257	907.27	33577	906.75	30605	906.83	24864
	3+	u^{I}	900.15	61680	901.97	18672	901.10	23720	900.40	38996
	4+	u	900.00	23924	900.63	26152	900.25	18293	900.17	17124
	3+	u_0	897.86	12028	898.70	5481	898.11	20836	897.76	6738
Ce $3d_{5/2}$	4+	v^{III}	897.22	69928	898.03	61852	897.58	53851	897.48	52257
	4+	v^{II}	888.01	42569	888.57	41412	888.01	40693	887.84	42443
	3+	v^{I}	882.86	97634	883.58	52005	883.56	46200	883.36	40018
	4+	v	881.42	46487	882.13	38497	881.82	50569	881.62	44643
	3+	v_0	879.59	3271	880.51	8908	880.49	8632	880.03	8470
O 1s	O_β		530.67	43927	531.37	45043	530.93	55772	530.95	58816
	O_α		528.49	82332	529.19	62847	528.85	65117	528.97	54437
Cu 2p	$2p_{3/2}$				932.83	33934	932.35	40094	932.37	39705
	$2p_{1/2}$				952.71	16550	952.25	20894	952.17	16776
%	Ce		17.24		16.40		15.61		16.96	
	O		82.76		77.06		77.00		74.50	
	Cu				6.54		7.39		8.54	

3.5. Optical analysis

The optical characteristics of pure and Cu-doped CeO_2 nanoparticles are determined by UV-Vis (DRS) measurements and the results are demonstrated in figure 13. The Kubelka-Munk function given by equation (3):

$$F(R) = \frac{(1-R)^2}{2R} \quad (3)$$

which includes the reflectance R obtained from the DRS spectra is used to determine the bandgap of

the samples. The graph plotted between $(F(R)h\upsilon)^2$ and photon energy ($h\upsilon$) relates to a direct bandgap transition, while $(F(R)h\upsilon)^{1/2}$ and photon energy ($h\upsilon$) relate to an indirect bandgap transition [41].

The synthesized CeO_2 NPs exhibit a direct bandgap energy of E_g = 3.05 eV. However, with the increase in Cu-doping in the samples (Cu 5%, Cu 10% and Cu 15%), it is found to decrease to 2.14, 2.12 and 2.04 eV, respectively. The blue shift in the absorbance edge in the doped samples can be due to the bands created by the dopant atoms [42]. The bandgap energy 'E_{g1}' in doped samples shows the existence of energy levels in "midgap states", which specifies the overlap between Ce^{4+} and the $4f^1$-$5d^1$ transition of Ce^{3+} [39,43]. With doping, the bandgap has decreased and it can be described by the creation of localized states within the bandgap due to oxygen vacancies and an increase in Ce^{3+} ion concentration [32,44].

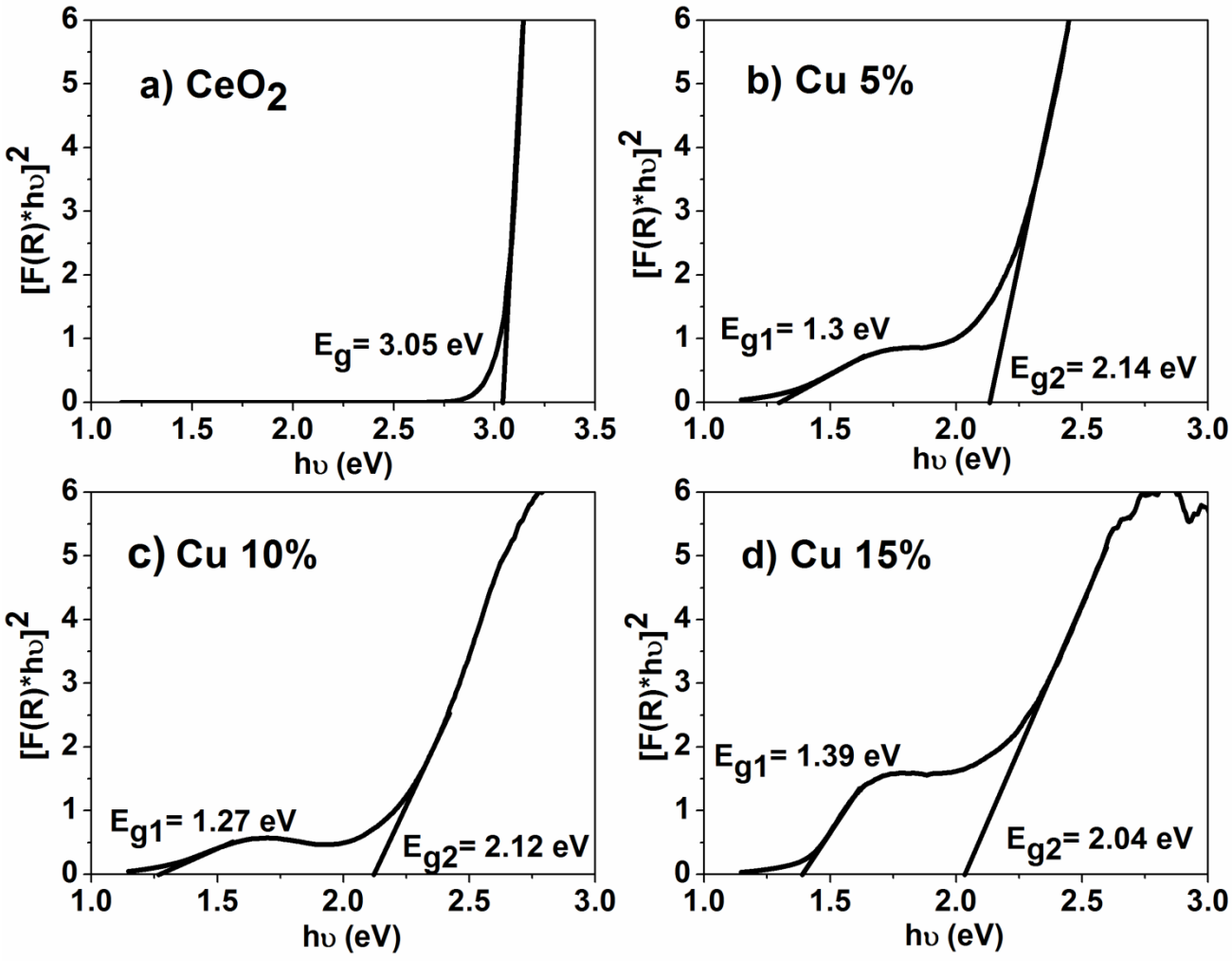

Figure 13. DRS spectra of CeO_2 NPs and Cu-doped CeO_2 NPs

3.6. Adsorption Studies

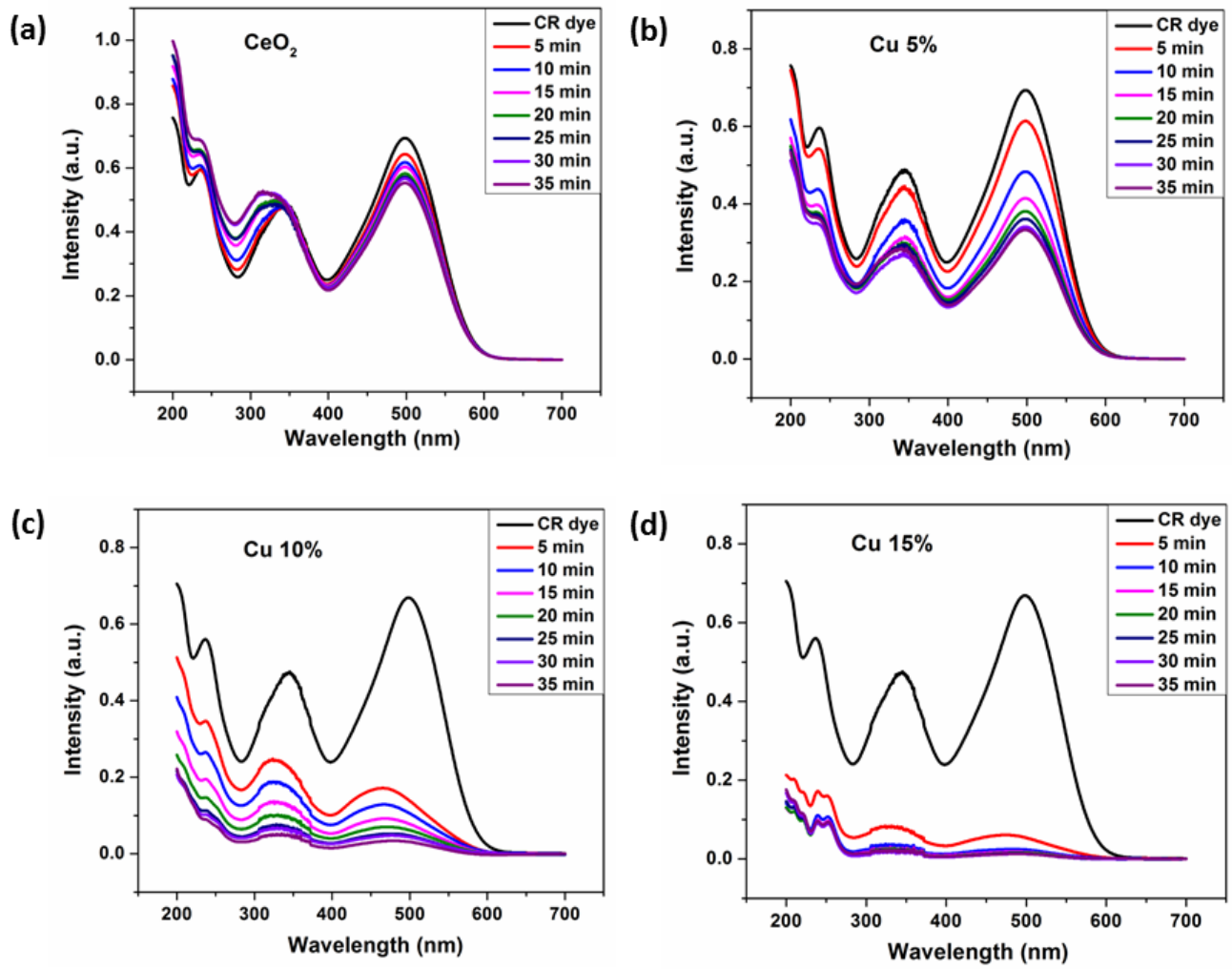

Figure 14. Absorbance spectra showing the adsorption removal of Congo red for CeO_2 NPs and Cu-doped CeO_2 NPs

In order to investigate the impact of copper doping on the adsorption capacity of Cu-doped CeO_2 NPs towards Congo red dye, a series of adsorption experiments are performed. The initial concentration of the dye is set at 1mg per 100ml. Figure 14 presents the absorption peaks of the dye at 5 minute intervals after the introduction of the adsorbent in the dye kept under dark conditions. The variations in the adsorption capacity for each sample are evident from the differences in the intensity of absorption peaks over time. For pure ceria, adsorption after 35 minute is very low, as shown by the absorption

peak intensity in Figure 14(a), whereas the adsorption capacity increases with the increase in copper dopant concentration from Cu 5% to Cu 15%.

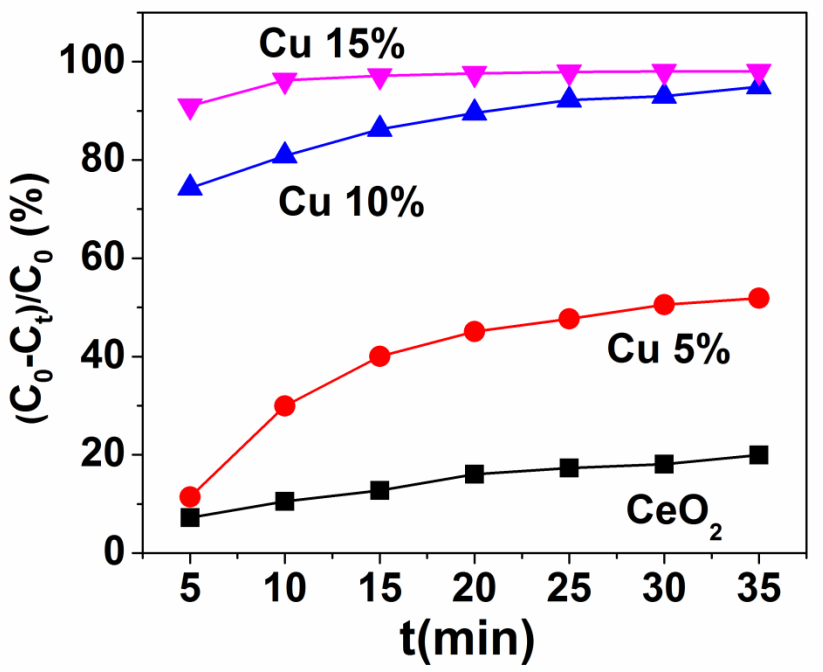

Figure 15. Plot of adsorptive removal capacity against time for CeO_2 NPs and Cu-doped CeO_2 NPs

Figure 15 demonstrate the percentage of dye removal efficiency for the four different samples against Congo red dye. The doped samples exhibit considerably higher removal efficiency compared to pure CeO_2. For instance, Cu 15% doped CeO_2 NPs exhibit 98% Congo red removal efficiency within 35 minutes, which remains unchange in the next five-minute interval. This is because a state of equilibrium has been attained as sorption sites in the sample get saturated with the ions of Congo red dye with time. In contrast, pure CeO_2, Cu 5% and Cu 10% exhibit percentage removal of 18,50 and 93%, respectively, in 35 minutes. The significant increase in removal efficiency observed in Cu10% and Cu15% can be attributed to changes in surface features resulting from the formation of the CuO phase and the introduction of more oxygen vacancies due to the reduction of Ce^{4+} to Ce^{3+}. To gain a deeper understanding of the adsorption mechanism and adsorption favorability of the samples, a detailed analysis of the adsorption kinetics and adsorption isotherm fits using different theoretical models are attempted.

The absorbance data after photocatalysis (supplementary information figure S1 and S2) clearly indicates that adsorption rather than photocatalytic degradation plays the key role in the removal of

dye by Cu-doped ceria, which is a very interesting observation. A similar study has been done by Mousavi-Kamazani *et al* [13] who conducted adsorption as well as photocatalysis (without keeping under dark) on Cu-doped CeO_2 nanostructures synthesized by sonochemical method. The 5 wt% doped sample showed adsorption as well as photocatalytic degradation efficiency of 99% in 45 minutes against methyl orange. However, there is no mention of centrifugation before taking absorbance measurements in their work and hence it is difficult to get a proper understanding of whether adsorption or photocatalysis plays the predominant role there.

3.6.1. Adsorption kinetics for Congo red

The rate of adsorption of Congo red dye by the samples can be calculated from the kinetic studies. The conventional way of modeling the adsorption process and calculating the adsorption kinetic parameters is through the linearized form of the models [45]. Among the various linearized kinetic models that are conventionally used to assess the rate of dye removal from wastewater using adsorbents, the most appropriate models to analyze the experimental data in this work are found to be Lagergren pseudo-first-order (PFO) and pseudo-second-order models (PSO). The best-fit model is determined based on the linear regression correlation coefficient R^2 values. R^2 is an estimate of the degree to which the linearized kinetic theoretical models match with the experimental data [46,47].

The Lagergren PFO model is more appropriate for low concentrations of solution and is described by equation (4):

$$\ln(Q_e - Q_t) = \ln Q_e - k_1 t \qquad (4)$$

where Q_e is the quantity of dye adsorbed at equilibrium and Q_t is the quantity adsorbed at time t (min) in mg/g. k_1 is the PFO rate constant. The slope and intercept of the best-fit line of the plot of $\ln(Q_e-Q_t)$ versus t yields the required parameters as, $k_1 = -m$ and $Q_e = \exp(b)$ for PFO where m = slope and b = intercept.

The PSO model, on the other hand, mostly depends on the quantity of solute adsorbed on the adsorbent surface and that adsorbed at equilibrium and is described by equation (5):

$$\frac{t}{Q_t} = \frac{1}{k_2 Q_e^2} + \frac{t}{Q_e} \qquad (5)$$

where k_2 is the PSO rate constant. The value of k_2 and Q_e are determined from the intercept and slope of the plot of t/Q_t versus t as $k_2 = m^2/b$ and $Q_e = m^{-1}$.

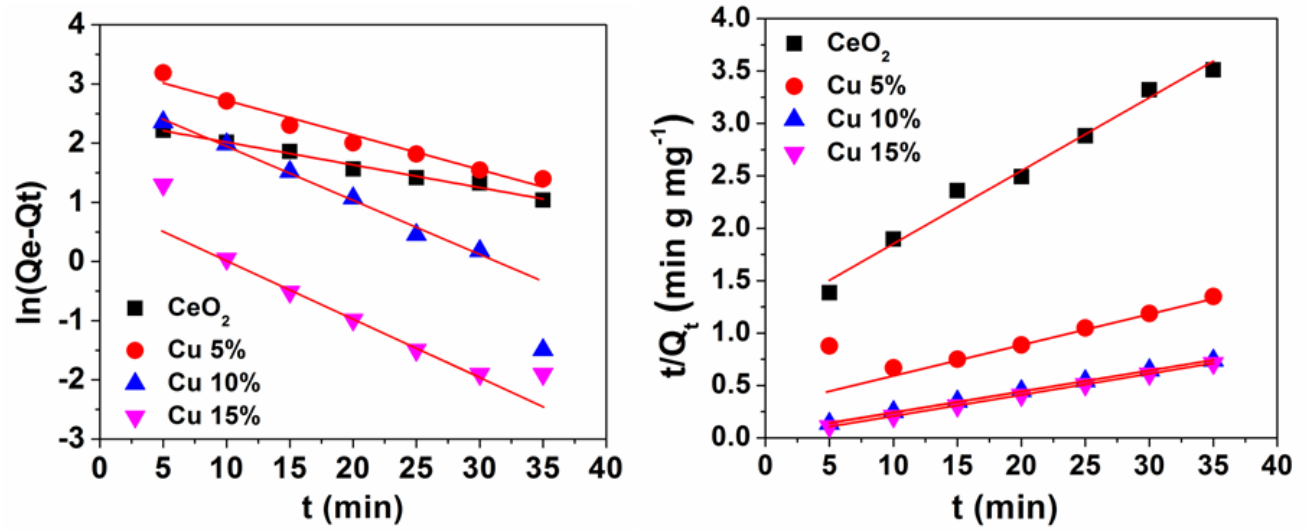

Figure 16. The linear plots of the (a) pseudo-first-order and (b) pseudo-second-order kinetic models of CeO_2 and Cu-doped CeO_2 NPs

Table 3. The determined kinetics parameters of PFO and PSO kinetic model with correlation coefficients (R^2) for CeO_2 and Cu-doped CeO_2 NPs

Sample	Pseudo-first-order				Pseudo-second-order		
	$Q_{e,exp}$(mg g^{-1})	k_1(min^{-1})	$Q_{e,cal}$(mg g^{-1})	R^2	k_2(gmg^{-1} min^{-1})	$Q_{e,cal}$(mg g^{-1})	R^2
CeO_2	12.7890	0.0384	11.0319	0.9850	0.0042	14.3534	0.9801
Cu 5%	29.9856	0.0585	27.3159	0.9591	0.0022	35.8938	0.9898
Cu 10%	47.6831	0.0910	17.2985	0.9915	0.0092	50.0250	0.9993
Cu 15%	49.1779	0.0975	2.6624	0.9965	0.0564	49.6032	0.9999

Figure 16 shows the linear plots of the PFO and PSO kinetic models at an initial concentration of 1mg

per 100ml. The estimated kinetics parameters are listed in Table 3. The adsorption capacity calculated (Qe,cal) from the PSO model is consistent with the experimental adsorption value (Qe,exp) compared to the PFO model for the doped samples. However, for pure ceria, the Qe,exp value of PFO is closer. The correlation coefficient is much greater for the PSO model than for PFO in the Cu-doped samples indicating that chemisorption is the rate-controlling step in the adsorption process of Congo red on Cu-doped CeO_2 NPs. This suggests that Cu doping plays a significant role in the adsorption kinetics of ceria. The amount of dye adsorbed at equilibrium is found to be very low in pure ceria, but it significantly increased in the Cu doped and is maximum in Cu15%, which corroborates the observation of high adsorption capacity of the latter.

3.6.2. Adsorption isotherm studies

Adsorption isotherm analysis is used to determine the maximum adsorption capacity of adsorbents against a specific species when the adsorption attains equilibrium. The adsorbent concentration is fixed at 1mg/5ml, and the amount of Congo red is altered (1, 2, 3 and 5 mg per 100ml). To explain the equilibrium adsorption isotherm, Langmuir and Freundlich isotherms are utilized to examine the equilibrium experimental data for the sorption of Congo red on Cu-doped CeO_2 NPs [48].

The Langmuir adsorption isotherm model conventionally best fits a homogeneous system with identical and energetically equivalent sorption sites. It represents a monolayer adsorption as no further adsorption can occur on a sorption site once it is occupied by an adsorbate. Langmuir assumed that the adsorbent surface has a finite number of sorption sites and there will be no interaction between the adsorbates occupying those sites [20,49]. The Langmuir isotherm is described by equation (6):

$$\frac{C_e}{Q_e} = \frac{C_e}{Q_m} + \frac{1}{k_L Q_m} \qquad (6)$$

where Q_e is the amount of dye adsorbed at equilibrium in mg/g, Q_m is the maximum uptake of adsorbate (i.e. monolayer saturation) in mg/g, C_e is the concentration of adsorbate at equilibrium in mg/L, and k_L is the Langmuir adsorption isotherm constant in L/mg. K_L represents the extent of interaction between the adsorbate and adsorbent (i.e. adsorption affinity). The Q_m and k_L values are determined from the slope and intercept of the linear C_e/Q_e versus C_e plot.

In Langmuir isotherm, a dimensionless factor called equilibrium parameter R_L quantifies the connection between adsorbent and adsorbate. It is defined as equation (7):

$$R_L = \frac{1}{1+k_L C_0} \quad (7)$$

Here, C_0 denotes the initial Congo red dye concentration in mg/L. An adsorption process can be classified into favorable and unfavorable adsorption, depending on the value of R_L. The value of R_L between 0 and 1 indicates favorable adsorption and R_L >1 or R_L=1 indicates unfavorable adsorption [12].

The Freundlich adsorption isotherm model accounts for a heterogeneous and multilayer system and the model is expressed as equation (8):

$$\log Q_e = \log k_F + \frac{1}{n} \log C_e \quad (8)$$

where k_F and n are Freundlich constants with k_F being the adsorbent capacity and n being the adsorption intensity. The values of k_F and 1/n are determined from the intercept and slope of the log C_e vs log Q_e linear plot. For a good adsorption process, the values of n should lie between 1.0 and 10.0 [48,50].

The plots drawn from the two linearized isotherm equations are given in figures 17 and figure 18. Table 4 shows the parameters calculated from the linear regression of the isotherms. From the figures, it is seen that the Langmuir isotherm is a best fit for the measured data than the Freundlich isotherm. This represents a monolayer adsorption of Congo red on the samples. Also, the R_L value lies between 0 and 1, indicating that the adsorption is favorable. The trend shown by Cu-doped samples for both K_L and Q_m suggests that Cu doping enhances the affinity of the dye molecules against the adsorbent and that they behave like a homogeneous adsorption system. The greater the percentage of Cu doping, the stronger the interaction. And this is reflected in the increase in Q_m value that indicates greater adsorption capacity for Cu-doped samples.

Table 4. Parameters for the two isotherm models

Sample	Langmuir isotherm				Freundlich isotherm		
	K_L (L/mg)	Q_m (mg/g)	R^2	R_L	K_F [mg/g (L/mg)]$^{1/n}$	n	R^2
CeO_2 CL	0.905	12	0.9986	0.5923	7.925	5.382	-0.3556
Cu 5%	0.071	58	0.9999	0.9487	7.745	1.972	0.7231
Cu 10%	0.128	194	0.9998	0.9110	49.888	2.798	0.2617
Cu 15%	2.062	193	0.9999	0.3892	149.279	1.682	0.7456

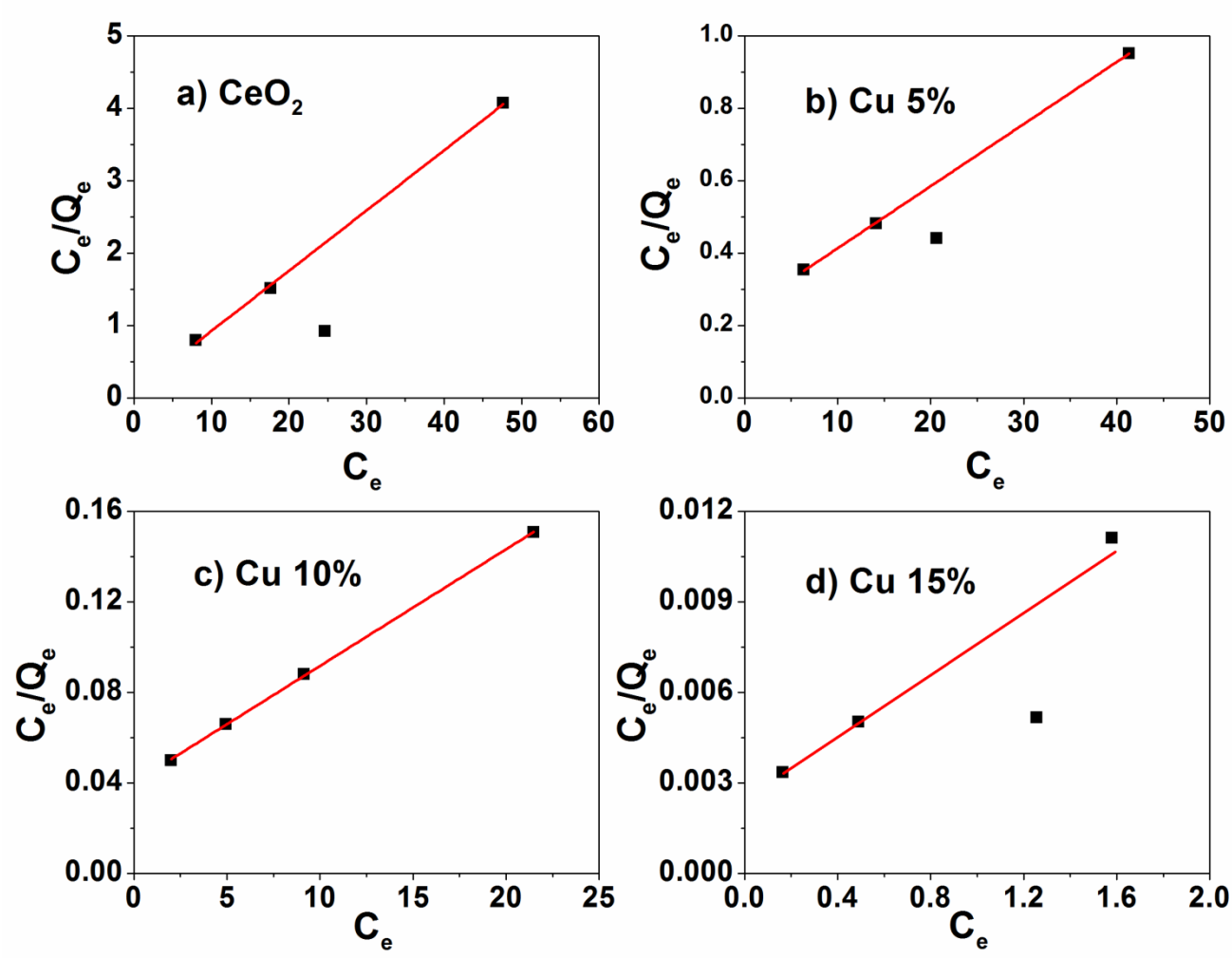

Figure 17. The linearly fitted Langmuir isotherm of CeO_2 and Cu-doped CeO_2 NPs

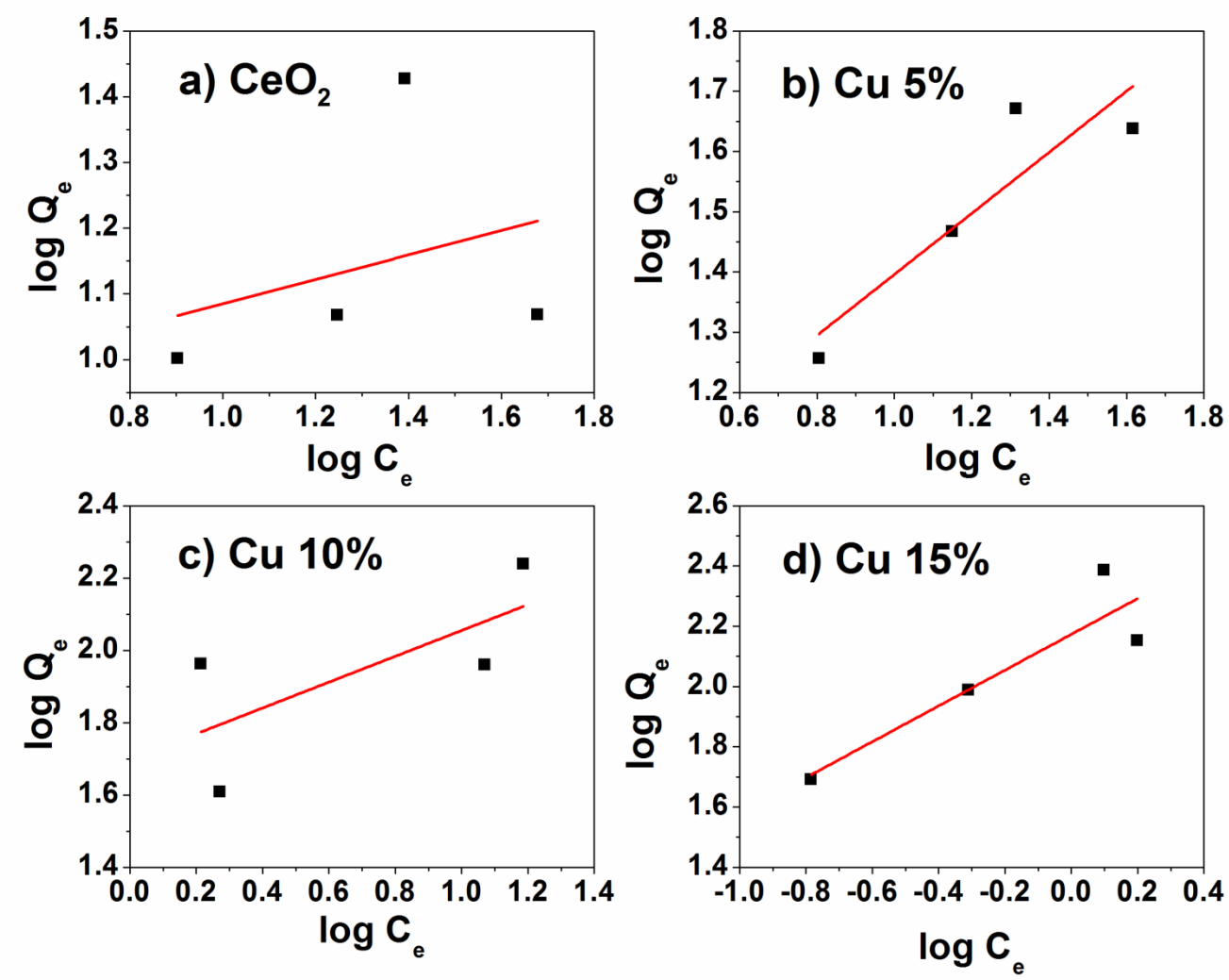

Figure 18. The linearly fitted Freundlich isotherm of CeO_2 and Cu-doped CeO_2 NPs

The enhanced adsorption capacity of Cu-doped samples is solely due to (i) changes in surface properties such as surface area, pore diameter and pore volume brought by Cu-doping compared to the pure CeO_2 NPs and (ii) the presence of surface oxygen vacancies in high density due to the replacement of Ce^{4+} ions with trivalent cations to maintain charge neutrality.

3.7. Antibacterial Studies

The antibacterial activity of pure and Cu-doped CeO_2-NPs against four bacterial strains, gram-positive bacteria *Staphylococcus aureus* and *Bacillus subtilis* and gram-negative bacteria *Pseudomonas*

aeruginosa and *Escherichia coli* are studied using well diffusion method. In all the plates the control has trivial activity against the bacterial strains. All the Cu-doped samples exhibited better antibacterial activity than pure CeO_2 against the four bacterial strains as seen in figure 19(a). The measured zone of inhibition (ZOI) for the samples against four bacterial strains represented in bar diagram is given in figure 19(b). CeO_2 NPs synthesized using aloe vera extract in our earlier work show no bacterial growth inhibition whereas in this present study using curry leaves extract, there is appreciable activity for pure CeO_2 NPs [22].

The antibacterial activity of the samples is primarily because of the oxidative stress induced by reactive oxygen species (ROS) and the reduction of Ce^{4+} to Ce^{3+}. The ROS generated in the samples leads to the tear down of bacterial cell wall membrane. The production of highly reactive species like hydroxyl radicals (·OH), singlet oxygen ($^1O_2$) and superoxide radicals (O_2^-) penetrate into the cell membrane and lead to the effusion of lipids, proteins and genetic materials, resulting in bacterial death [29]. The measured ZOI reveals that inhibition values increase with the increase in copper dopant concentration, due to the rise in the concentration of ROS on the surface of NPs. The possible chemical reactions of ROS production are given as in equations (9)-(15):

$$CeO_2 + h\upsilon \rightarrow e^- + h^+ \quad (9)$$

$$h^+ + H_2O \rightarrow \cdot OH + H^+ \quad (10)$$

$$e^- + O_2 \rightarrow O_2^- \quad (11)$$

$$O_2^- + H^+ \rightarrow HO_2\cdot \quad (12)$$

$$2HO_2\cdot \rightarrow H_2O_2 + O_2 \quad (13)$$

$$HO_2\cdot + H^+ + e^- \rightarrow H_2O_2 \quad (14)$$

$$H_2O_2 + e^- \rightarrow \cdot OH + OH^- \quad (15)$$

The improved antibacterial activity of copper-doped ceria over pure ceria can be attributed to the i) decrease in bandgap energy with increased production of ROS, ii) formation of more number of oxygen vacancies that arises from Cu^{2+} substitution at Ce sites and iii) the quick switching between Ce^{4+} and Ce^{3+} with Cu doping [22].

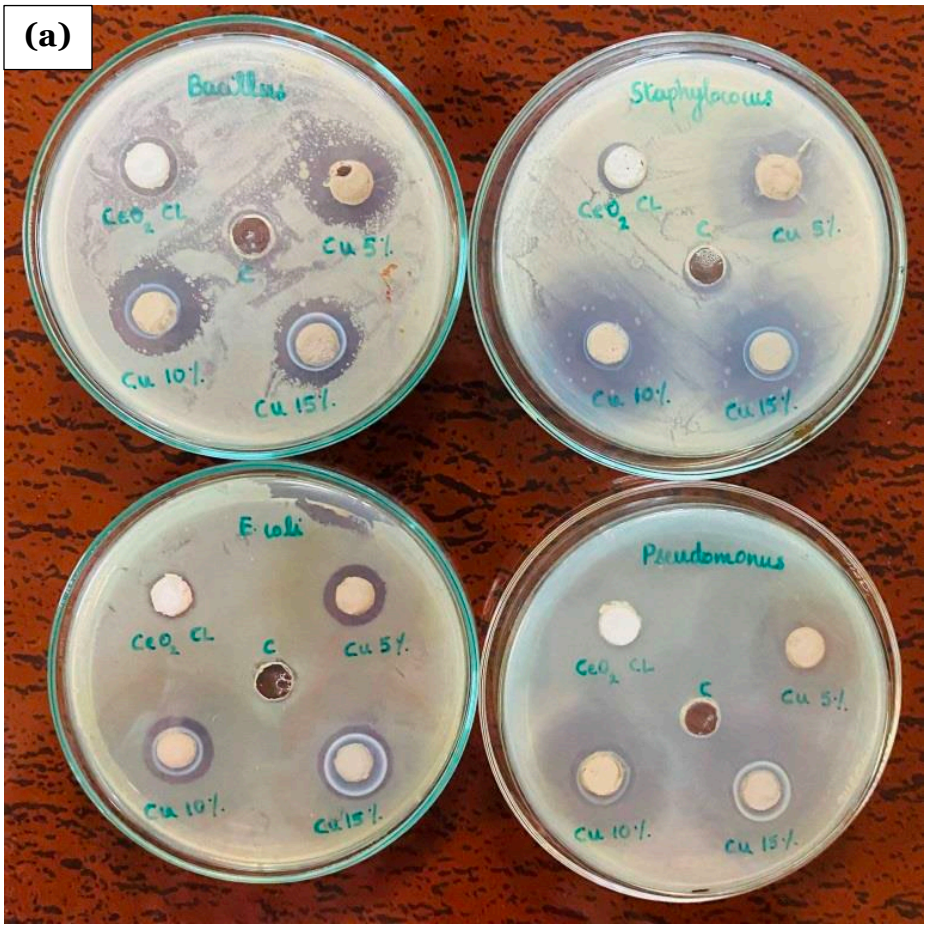

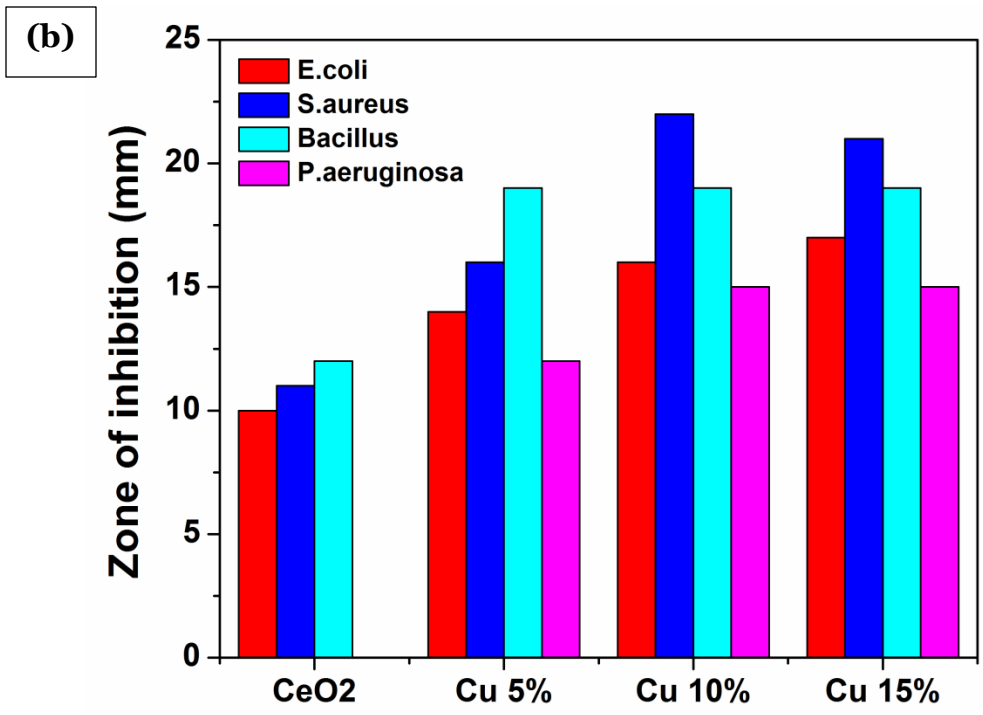

Figure 19. (a) Zone of inhibition and (b) bar graph showing the measured zone of inhibition for CeO_2 and Cu-doped CeO_2 NPs against four different bacterial strains

4. Conclusions

Copper-doped CeO_2 NPs with different concentrations of Cu ions (0, 5, 10 and 15 wt%) with enhanced adsorption and antibacterial activity are successfully synthesized via a green route using *Murraya Koenigii* (curry) leaves extract for the first time. The effect of different Cu concentrations on pure ceria are analyzed using XRD, FESEM, TEM, BET, FTIR, Raman spectroscopy, XPS and DRS to understand its surface characteristics and adsorption capacity towards Congo red dye and its antibacterial action on different pathogens. The main findings are as follows.

(i) The percentage of dye removal by adsorption is found to be improving with doping from 18% for pure ceria to 50%, 93% and 98% in 35 minutes respectively for Cu 5% , Cu 10% and Cu 15% doped ceria.

(ii) Cu 15% doped CeO_2 NPs are the most efficient adsorbents for Congo red, exhibiting an adsorption efficiency of 193 mg/g.

(iii) The adsorption kinetics study estimated by the PFO and PSO models shows that PSO is more suited for its reaction with an R^2 value of 0.9999 indicating the chemical nature of adsorption.

(iv) The Langmuir isotherms data with R^2 value of 0.9999 indicate homogeneous monolayer adsorption. The increase in Cu-dopant concentration results in an increase in the number of adsorption sites due to changes in the surface characteristics as evident in FESEM.

(v) The Cu-doped CeO_2 NPs have superior antibacterial activity against the gram-positive bacteria *Bacillus subtilis* and *Staphylococcus aureus* and gram-negative bacteria *Escherichia coli* and *Pseudomonas aeruginosa*.

(vi) The enhanced number of Ce^{3+} states, oxygen vacancies and reactive oxygen species generated upon Cu-doping into the CeO_2 lattice play an important role in its improved adsorptive and antibacterial activity.

(vii) These findings suggest that the green synthesized copper-doped CeO_2 NPs have promising potential as antibacterial agents and adsorbents for dye removal in wastewater treatments.

Acknowledgments

The authors are grateful to DST-SERB for funding through a major research project (Ref. No. CRG/2020/000448). The corresponding and first author would like to acknowledge Dr. Johns Naduvath, Assistant Professor and Shanu Ananthath, Research Scholar, Department of Physics, St. Thomas College, Pala for XRD measurements and STIC, CUSAT for HRTEM, FTIR and DRS measurements.

Conflict of interest

There are no conflicts to declare.

Data availability statement

The data that support the findings of this study are available upon request from the authors.

References

[1] Ikram M, Umar E, Raza A, Haider A, Naz S, Ul-Hamid A, Haider J, Shahzadi I, Hassan J and

Ali S 2020 Dye degradation performance, bactericidal behavior and molecular docking analysis of Cu-doped TiO 2 nanoparticles *RSC Adv.* **10** 24215–33

[2] Andish-Lifshagerd F, Habibi-Yangjeh A, Habibi M and Akinay Y 2024 Facile synthesis of ZnO/CeO2/CeFeO3 photocatalysts sensitive to visible light with tandem n-n heterojunctions and improved performance towards tetracycline and dye effluent removals *J. Photochem. Photobiol. A Chem.* **448** 115351

[3] Litefti K, Freire M S, Stitou M and González-Álvarez J 2019 Adsorption of an anionic dye (Congo red) from aqueous solutions by pine bark *Sci. Rep.* **9** 16530

[4] Kumari H, Suman S, Ranga R and Chahal S 2023 *A Review on Photocatalysis Used For Wastewater Treatment : Dye Degradation* (Springer International Publishing)

[5] Hynes N R J, Kumar J S, Kamyab H, Sujana J A J, Al-Khashman O A, Kuslu Y, Ene A and Suresh Kumar B 2020 Modern enabling techniques and adsorbents based dye removal with sustainability concerns in textile industrial sector -A comprehensive review *J. Clean. Prod.* **272** 122636

[6] Singh A, Pal D B, Mohammad A, Alhazmi A, Haque S, Yoon T, Srivastava N and Gupta V K 2022 Biological remediation technologies for dyes and heavy metals in wastewater treatment: New insight *Bioresour. Technol.* **343** 126154

[7] Tan K B, Vakili M, Horri B A, Poh P E, Abdullah A Z and Salamatinia B 2015 Adsorption of dyes by nanomaterials: Recent developments and adsorption mechanisms *Sep. Purif. Technol.* **150** 229–42

[8] Wang L, Shi C, Wang L, Pan L, Zhang X and Zou J-J 2020 Rational design, synthesis, adsorption principles and applications of metal oxide adsorbents: a review *Nanoscale* **12** 4790–815

[9] Dutta S, Gupta B, Srivastava S K and Gupta A K 2021 Recent advances on the removal of dyes from wastewater using various adsorbents: a critical review *Mater. Adv.* **2** 4497–531

[10] Kurian M 2020 Cerium oxide based materials for water treatment – A review *J. Environ. Chem. Eng.* **8** 104439

[11] Singh K R B, Nayak V, Sarkar T and Singh R P 2020 Cerium oxide nanoparticles: Properties, biosynthesis and biomedical application *RSC Adv.* **10** 27194–214

[12] Joshy D, Chakko S, Ismail Y A and Periyat P 2021 Nanoscale Advances Surface basicity mediated rapid and selective adsorptive removal of Congo red over 6704–18

[13] Mousavi-Kamazani M and Azizi F 2019 Facile sonochemical synthesis of Cu doped CeO2 nanostructures as a novel dual-functional photocatalytic adsorbent *Ultrason. Sonochem.* **58** 104695

[14] Nyabadza A, McCarthy É, Makhesana M, Heidarinassab S, Plouze A, Vazquez M and Brabazon D 2023 A review of physical, chemical and biological synthesis methods of bimetallic nanoparticles and applications in sensing, water treatment, biomedicine, catalysis and hydrogen storage *Adv. Colloid Interface Sci.* **321** 103010

[15] Baig N, Kammakakam I and Falath W 2021 Nanomaterials: a review of synthesis methods, properties, recent progress, and challenges *Mater. Adv.* **2** 1821–71

[16] Sharma A, Pal K, Saini N, Kumar S, Bansal D and Mona S 2023 Remediation of contaminants from wastewater using algal nanoparticles via green chemistry approach: an organized review *Nanotechnology* **34** 352001

[17] SI A, Pal K, Kralj S, El-Sayyad G S, de Souza F G and Narayanan T 2020 Sustainable preparation of gold nanoparticles via green chemistry approach for biogenic applications *Mater. Today Chem.* **17** 100327

[18] Md Ishak N A I, Kamarudin S K and Timmiati S N 2019 Green synthesis of metal and metal oxide nanoparticles via plant extracts: an overview *Mater. Res. Express* **6**

[19] Chakroborty S, Nath N and Pal K 2022 Limitations of nanomaterials insights in green chemistry sustainable route: Review on novel applications *Green Process. Synth.* **11** 951–64

[20] Sharma A, Mittal R, Sharma P, Pal K and Mona S 2023 Sustainable approach for adsorptive removal of cationic and anionic dyes by titanium oxide nanoparticles synthesized biogenically using algal extract of Spirulina *Nanotechnology* **34** 485301

[21] Pal K, Chakroborty S, Panda P, Nath N and Soren S 2022 Environmental assessment of wastewater management via hybrid nanocomposite matrix implications—an organized review *Environ. Sci. Pollut. Res.* **29** 76626–43

[22] Norbert A, Alappatt S M, John S S, Shaji S, Remillard S K, Deshpande U P and Reena Philip R 2023 Phytosynthesized Cu-Doped Cerium Oxide Nanoparticles for Antibacterial Application *Phys. status solidi* **220** 2200731

[23] Kaur R, Kaushal S and Singh P P 2020 Biogenic synthesis of a silver nanoparticle–SnZrMoP nanocomposite and its application for the disinfection and detoxification of water *Mater. Adv.* **1** 728–37

[24] Arumugam A, Karthikeyan C, Haja Hameed A S, Gopinath K, Gowri S and Karthika V 2015 Synthesis of cerium oxide nanoparticles using Gloriosa superba L. leaf extract and their structural, optical and antibacterial properties *Mater. Sci. Eng. C* **49** 408–15

[25] Eka Putri G, Rilda Y, Syukri S, Labanni A and Arief S 2021 Highly antimicrobial activity of cerium oxide nanoparticles synthesized using Moringa oleifera leaf extract by a rapid green precipitation method *J. Mater. Res. Technol.* **15** 2355–64

[26] N B R, T P G N, S P O, K S S, B P, P N H, R A K M, S S B, R S S T and C P S 2021 Eco-friendly synthesis of CeO2 NPs using Aloe barbadensis Mill extract: Its biological and photocatalytic activities for industrial dye treatment applications *J. Photochem. Photobiol.* **7** 100038

[27] Magudieshwaran R, Ishii J, Raja K C N, Terashima C, Venkatachalam R, Fujishima A and Pitchaimuthu S 2019 Green and chemical synthesized CeO2 nanoparticles for photocatalytic indoor air pollutant degradation *Mater. Lett.* **239** 40–4

[28] Yiling W, Murakonda G K and Jarubula R 2021 Application of green-synthesized cerium oxide nanoparticles to treat spinal cord injury and cytotoxicity evaluation on paediatric leukaemia cells *Mater. Res. Express* **8** 075006

[29] Satheshkumar M, Anand B, Muthuvel A, Rajarajan M, Mohana V and Sundaramanickam A 2020 Enhanced photocatalytic dye degradation and antibacterial activity of biosynthesized ZnO-NPs using curry leaves extract with coconut water *Nanotechnol. Environ. Eng.* **5**

[30] Zheng N, Wang Z, Long J, Kong L, Chen D and Liu Z 2018 Journal of Colloid and Interface Science Shape-dependent adsorption of CeO 2 nanostructures for superior organic dye removal *J. Colloid Interface Sci.* **525** 225–33

[31] Magdalane C M, Kaviyarasu K, Vijaya J J, Siddhardha B and Jeyaraj B 2016 Photocatalytic activity of binary metal oxide nanocomposites of CeO2/CdO nanospheres: Investigation of optical and antimicrobial activity *J. Photochem. Photobiol. B Biol.* **163** 77–86

[32] Ranjith K S, Dong C L, Lu Y R, Huang Y C, Chen C L, Saravanan P, Asokan K and Rajendra Kumar R T 2018 Evolution of Visible Photocatalytic Properties of Cu-Doped CeO2 Nanoparticles: Role of Cu2+-Mediated Oxygen Vacancies and the Mixed-Valence States of Ce Ions *ACS Sustain. Chem. Eng.* **6** 8536–46

[33] Kumari K, Aljawfi R N, Chawla A K, Kumar R, Alvi P A, Alshoaibi A, Vij A, Ahmed F, Abu-samak M and Kumar S 2020 Engineering the optical properties of Cu doped CeO2 NCs for

application in white LED *Ceram. Int.* **46** 7482–8

[34] Dutta D, Mukherjee R, Patra M, Banik M, Dasgupta R, Mukherjee M and Basu T 2016 Green synthesized cerium oxide nanoparticle: A prospective drug against oxidative harm *Colloids Surfaces B Biointerfaces* **147** 45–53

[35] Sudarsanam P, Hillary B, Amin M H, Rockstroh N, Bentrup U, Brückner A and Bhargava S K 2018 Heterostructured Copper-Ceria and Iron-Ceria Nanorods: Role of Morphology, Redox, and Acid Properties in Catalytic Diesel Soot Combustion *Langmuir* **34** 2663–73

[36] Su Y, Dai L, Zhang Q, Li Y, Peng J, Wu R, Han W, Tang Z and Wang Y 2016 Fabrication of Cu-Doped CeO2 Catalysts with Different Dimension Pore Structures for CO Catalytic Oxidation *Catal. Surv. from Asia* **20** 231–40

[37] Elango M, Deepa M, Subramanian R and Mohamed Musthafa A 2018 Synthesis, Characterization, and Antibacterial Activity of Polyindole/Ag–Cuo Nanocomposites by Reflux Condensation Method *Polym. Plast. Technol. Eng.* **57** 1440–51

[38] Ethiraj A S and Kang D J 2012 Synthesis and characterization of CuO nanowires by a simple wet chemical method *Nanoscale Res. Lett.* **7** 70

[39] Calvache-Muñoz J, Prado F A and Rodríguez-Páez J E 2017 Cerium oxide nanoparticles: Synthesis, characterization and tentative mechanism of particle formation *Colloids Surfaces A Physicochem. Eng. Asp.* **529** 146–59

[40] Sing K S W 1985 Reporting physisorption data for gas/solid systems with special reference to the determination of surface area and porosity (Recommendations 1984) *Pure Appl. Chem.* **57** 603–19

[41] Joseph J A, Nair S B, John K A, Babu S, Shaji S, Shinoj V K and Philip R R 2020 Aluminium doping in iron oxide nanoporous structures to tailor material properties for photocatalytic applications *J. Appl. Electrochem.* **50** 81–92

[42] Magdalane C M, Kaviyarasu K, Vijaya J J, Siddhardha B, Jeyaraj B, Kennedy J and Maaza M 2017 Evaluation on the heterostructured CeO2/Y2O3 binary metal oxide nanocomposites for UV/Vis light induced photocatalytic degradation of Rhodamine - B dye for textile engineering application *J. Alloys Compd.* **727** 1324–37

[43] Maria Magdalane C, Kaviyarasu K, Judith Vijaya J, Jayakumar C, Maaza M and Jeyaraj B 2017 Photocatalytic degradation effect of malachite green and catalytic hydrogenation by UV–illuminated CeO2/CdO multilayered nanoplatelet arrays: Investigation of antifungal and

antimicrobial activities *J. Photochem. Photobiol. B Biol.* **169** 110–23

[44] Elaziouti A, Laouedj N, Bekka A and Vannier R N 2015 Preparation and characterization of p-n heterojunction CuBi2O4/CeO2 and its photocatalytic activities under UVA light irradiation *J. King Saud Univ. - Sci.* **27** 120–35

[45] Revellame E D, Lord D, Sharp W, Hernandez R and Zappi M E 2020 Adsorption kinetic modeling using pseudo- fi rst order and pseudo-second order rate laws : A review *Clean. Eng. Technol.* **1** 100032

[46] Zheng Y, Wang H, Cheng B, You W and Yu J 2018 Fabrication of hierarchical bristle-grass-like NH 4 Al (OH) 2 CO 3 @ Ni (OH) 2 core-shell structure and its enhanced Congo red adsorption performance *J. Alloys Compd.* **750** 644–54

[47] Guo H, Ke Y and Wang D 2013 Efficient adsorption and photocatalytic degradation of Congo red onto hydrothermally synthesized NiS nanoparticles

[48] Kalam S, Abu-Khamsin S A, Kamal M S and Patil S 2021 Surfactant Adsorption Isotherms: A Review *ACS Omega* **6** 32342–8

[49] Zito P and Shipley H J 2015 Inorganic nano-adsorbents for the removal of heavy metals and arsenic: a review *RSC Adv.* **5** 29885–907

[50] Wu X, Wang W, Li F, Khaimanov S, Tsidaeva N and Lahoubi M 2016 PEG-assisted hydrothermal synthesis of CoFe2O4 nanoparticles with enhanced selective adsorption properties for different dyes *Appl. Surf. Sci.*